Monthly Notices
of the
ROYAL ASTRONOMICAL SOCIETY

MNRAS **463,** 45–62 (2016)
Advance Access publication 2016 August 4

doi:10.1093/mnras/stw1934

Transiting planet candidates with ASTEP 400 at Dome C, Antarctica

D. Mékarnia,[1⋆] T. Guillot,[1⋆] J.-P. Rivet,[1] F.-X. Schmider,[1] L. Abe,[1] I. Gonçalves,[1] A. Agabi,[1] N. Crouzet,[2] T. Fruth,[3,4] M. Barbieri,[5] D. D. R. Bayliss,[6] G. Zhou,[6] E. Aristidi,[1] J. Szulagyi,[1] J.-B. Daban,[1] Y. Fanteï-Caujolle,[1] C. Gouvret,[1] A. Erikson,[3] H. Rauer,[3] F. Bouchy,[7] J. Gerakis[1] and G. Bouchez[8]

[1]*Université Côte d'Azur, Observatoire de la Côte d'Azur, CNRS, Lagrange, Boulevard de l'Observatoire, CS 34229, F-06304 Nice Cedex 4, France*
[2]*Dunlap Institute for Astronomy & Astrophysics, University of Toronto, 50 St. George Street, Toronto, ON M5S 3H4, Canada*
[3]*Institut für Planetenforschung, Deutsches Zentrum für Luft- und Raumfahrt, Rutherfordstr. 2, D-12489 Berlin, Germany*
[4]*German Space Operations Center, Deutsches Zentrum für Luft- und Raumfahrt, Münchener Strasse 20, D-82234 Weßling, Germany*
[5]*Department of Physics, University of Atacama, Copayapu 485, Copiapo, Chile*
[6]*Research School of Astronomy and Astrophysics, Australian National University, Canberra, ACT 2611, Australia*
[7]*Laboratoire d'Astrophysique de Marseille, AMU, CNRS, F-13388 Marseille, France*
[8]*GEMAC, Université de Versailles, CNRS, 45 av. des Etats-Unis, F-78035 Versailles Cedex, France*

Accepted 2016 August 2. Received 2016 August 2; in original form 2015 August 13

ABSTRACT

ASTEP 400, the main instrument of the ASTEP (Antarctica Search for Transiting ExoPlanets) programme, is a 40 cm telescope, designed to withstand the harsh conditions in Antarctica, achieving a photometric accuracy of a fraction of millimagnitude on hourly time-scales for planet-hosting southern bright ($R \sim 12$ mag) stars. We review the performances of this instrument, describe its operating conditions, and present results from the analysis of observations obtained during its first three years (2010–2012) of operation, before its repatriation in 2014. During this time, we observed a total of 22 stellar fields ($1^\circ \times 1^\circ$ field of view). Each field, in which we measured stars up to magnitude $R = 18$ mag, was observed continuously during ∼7 to ∼30 d. More than 200 000 frames were recorded and 310 000 stars processed, using an implementation of the optimal image subtraction photometry algorithm. We found 43 planetary transit candidates. 20 of these candidates were observed using spectroscopic follow-ups including four targets classified as good planet candidates. Our results demonstrate that accurate near-continuous photometric observations are achievable from the Concordia station at Dome C in Antarctica, even if we were not able to reach the nominal photometric precision of the instrument. We conducted a correlation analysis between the rms noise and a large number of external parameters and found that source of the ∼1 mmag correlated noise is not obvious and does not depend on a single parameter. However, our analysis provided some hints and guidance to increase the photometric accuracy of the instrument. These improvements should equip any future telescope operating in Antarctica.

Key words: instrumentation: photometers – methods: data analysis – methods: observational – planetary systems.

1 INTRODUCTION

Dome C, on the East Antarctic plateau, is one of the most promising sites for visible, infrared and sub-millimetre astronomy. An extensive range of wintertime measurements of the atmospheric turbulence have been made over this site revealing a very low cloud cover sky, an exceptional seeing above a thin boundary layer, very low wind speeds (Aristidi et al. 2003, 2005, 2009; Lawrence et al. 2004; Fossat et al. 2010; Giordano et al. 2012), a very low scintillation noise leading to superior photometric precision measurements (Kenyon et al. 2006), a high duty cycle (Mosser & Aristidi 2007; Moore et al. 2008; Crouzet et al. 2010) and a low sky brightness and extinction (Kenyon & Storey 2006). Dome C optical photometry was highlighted by several authors (Kenyon et al. 2006; Rauer, Fruth & Erikson 2008; Strassmeier et al. 2008; Abe et al. 2013; Crouzet et al. 2013). Dome A, another promising site on the Antarctic plateau, may also provide such favourable conditions (Bonner

⋆ E-mail: mekarnia@oca.eu (DM); guillot@oca.eu (TG)

et al. 2010; Wang et al. 2011). Furthermore, polar sites have the following obvious advantages leading to perform long and continuous time series observations: (i) a quasi-continuous astronomical darkness for about 4 months, for instruments exploiting the visible and NIR spectral bands, longer wavelengths being observed continuously year-round, and (ii) limited changes in the elevation of a large fraction of the observed sources.

The ASTEP (Antarctica Search for Transiting ExoPlanets) programme comprises two instruments: ASTEP South, a fixed 10 cm, $3\overset{\circ}{.}9 \times 3\overset{\circ}{.}9$ field of view (FoV) refractor pointed towards the celestial South Pole (Crouzet et al. 2010), and the ASTEP 400 telescope, a 40 cm Newton reflector with a $1^\circ \times 1^\circ$ FoV (Daban et al. 2010; Guillot et al. 2015). Both instruments are dedicated to find and characterize transiting exoplanets, although ASTEP South, as a precursor, was mainly used to probe the photometric capabilities of the site (Crouzet et al. 2010). These instruments use facilities provided by the French-Italian Antarctic station Concordia, located at Dome C (75°06′S, 123°21′E) at an altitude of 3233 m, 1100 km inland from the nearest coast. ASTEP South was installed in 2008 whereas ASTEP 400, subject of this paper, was installed in 2009 December and has operated from 2010 to 2013. After the end of the summer campaign 2013, the instrument was shipped back to Nice, in France.

We present here the ASTEP 400 instrument and the exoplanetary transit candidates resulting from the analysis of the 2010–2012 years. We first review the characteristics of the instrument, its performances, and describe its operating conditions as well as the observation strategy. Section 4 describes the data processing, the steps followed to perform high-precision time series photometry and the noise analysis. In Section 5, we present the transit search method and the follow-up observations of a sample of our exoplanet transit candidates. We report some properties for these transit candidates in Section 6 and summarize our results in Section 7.

2 INSTRUMENTATION

2.1 Telescope and focal box

ASTEP 400 is a custom 40 cm Newtonian telescope with a sophisticated field corrector, designed to withstand both Dome C summer and winter temperatures ranging from −20°C to −80°C with rapid variations (Daban et al. 2010). The primary mirror diameter is 40 cm with a focal ratio of 4.6. Because of its wide FoV ($1^\circ \times 1^\circ$) and of the layout of the optics and cameras in the focal box, the secondary mirror is quite big (23.5 cm × 16.5 cm) leading to a central obstruction of 42 per cent in radius (18 per cent in surface). Both primary and secondary mirrors are made in glass ceramic material Zerodur® and coated with protected aluminium. Even if a better reflectivity is provided with silver coatings in the red, we choose aluminium because it provides enhanced protection in harsh environment. Another important aspect is that recoating a mirror is impossible on site and we do not have any experience with silver coating in such harsh climatic conditions. Protected silver is generally more fragile than aluminium, in particular in the presence of condensation. However, people used to believe that the absence of dust and the low vapour content would prevent the coating degradation (Ashley et al. 2004). No experiment has been undertaken so far to check that assumption. Therefore, we preferred a more conservative approach for ASTEP. The mechanical structure of the telescope is an eighth-order Serrurier truss with carbon fibre legs, connected to an aluminium alloy main frame through Invar™ sleeves to achieve a good thermal and mechanical stability of the instrument (Fig. 1).

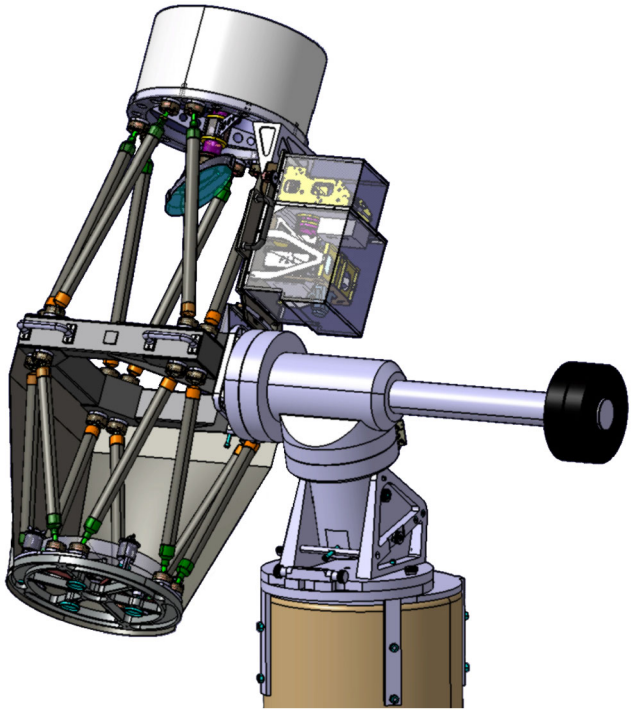

Figure 1. Engineering model of ASTEP 400. The mechanical structure of the telescope is an eighth-order Serrurier truss. The main frame in the middle of the structure and both its upper (the secondary mirror spider assembly) and lower part (the primary mirror barrel assembly) are made of aluminium. The hollow bars that link these three parts are made of carbon fibre with Invar™ sleeves at each end. The telescope mount is a commercial equatorial AP3600 from Astro-Physics Inc. that we have adapted to withstand the harsh Antarctic conditions.

The telescope structure is covered by a two-layer envelope to protect optics both against stray lights and ice dust deposit. Finite element analysis was carried out to predict the deformations of the structure depending on the telescope positions and temperature variations and their impact on the point spread function (PSF) quality and stability. Even with this careful design and manufacturing, the thermal expansion during rapid temperature variations may yield a telescope defocus of ∼150 μm for a temperature variation of 30°C (Guillot et al. 2015), with a telescope focal length of 1860 mm. This is equivalent to a PSF full width at half-maximum (FWHM) widening of 50 per cent.

The telescope and the focal box camera were designed, developed and constructed by our team, while the telescope mount is a commercial equatorial AP 3600 from Astro-Physics Inc. that we have adapted to the harsh Antarctic conditions (e.g., by changing the grease, heating the drive motors and by modifying a few mechanical components). Since the telescope is observing almost continuously, the mount is re-winded automatically, when it exceeds two or three spins, to prevent winding of the connection cables.

Fig. 2 illustrates the design of the focal box, which is divided into two compartments. The first compartment contains only optical components, the dichroic plate (D) and M3 mirror, while the second compartment contains the 'science/guiding' cameras, the motorized translation stage and their electronics. The focal box receives the incoming beam from the Newtonian telescope's flat secondary mirror through the two first lenses of the five-lens Wynne coma corrector, which act as a double-glazed insulation window. These lenses, along with the three other lenses located between the dichroic plate

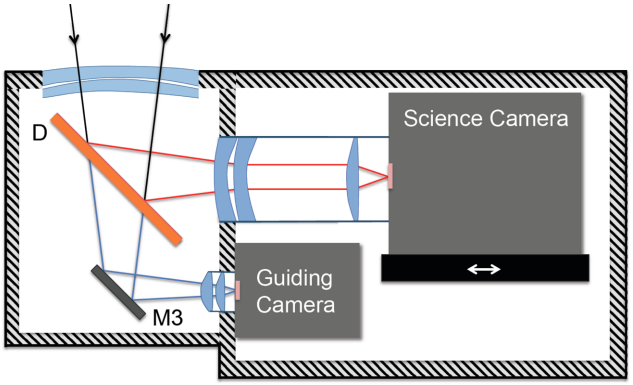

Figure 2. Optical design of the focal box. Light coming from the Newtonian flat secondary mirror through the double-glazed optical window is split into two beams by the dichroic plate (D) which reflects the red part to the Science camera and transmits the blue part to the Guiding camera through the mirror M3. The two first lenses of the optical window, along with the three other lenses, located between the dichroic plate and the Science camera, contribute to the field coma correction. The Science camera is mounted on a remote-controlled translation stage to get the proper focus.

and the Science camera, contribute to the field correction yielding an excellent image quality over the $1^\circ \times 1^\circ$ FoV. The PSF deformation across the field is negligible compared to the mean FWHM which is of 2 arcsec in good seeing conditions.

The focal box is mounted on a carbon fibre plate ensuring its rigidity and thermal stability. The opto-mechanical mounts are in titanium alloy chosen for its low weight, high mechanical resistance and low thermal expansion coefficient. The dichroic plate (D) separates the Science path from the telescope guiding path. The red part of the spectrum ($\lambda > 0.6$ μm) is sent to the Science camera, while the blue part ($\lambda < 0.6$ μm) is directed to the Guiding camera. No filter is used and most of the signal is transmitted in the red. The Science camera is a 4096 × 4096 pixels front-illuminated FLI Proline KAF 16801E CCD with a 16 bits analogue-to-digital converter. The CCD dimension is 36.8 mm × 36.8 mm and the plate scale is 0.93 arcsec pixel^{-1} (1 pixel = 9 μm). The Science camera, which is cooled by a Peltier device, is mounted on a MICOS® remote-controlled translation stage, which has a positioning accuracy better than 1 μm. In practice, the optical best-focus estimation cannot be better than 5 μm. The system was designed to be slightly defocused and spread the PSF FWHM to about 3 pixels reducing the noise due to jitter and inter-pixel variations. The actual optical train suffered an on-axis astigmatism that did not allow PSF FWHMs better than 2 arcsec; thus, no defocusing was necessary. On the contrary, this astigmatism was used to find the right focusing direction (inward or outward). The Science camera can be removed and replaced with an He–Ne laser for the optical alignment of the whole instrument. The optical combination has been calculated to ensure a stable and homogeneous PSF from the centre to the corners of the CCD, with an FWHM below 3 pixels when atmospheric turbulence is low and stable. This is not always the case because the entrance telescope pupil is at about 2 m above the ice surface, which is far from optimal seeing conditions at Dome C (Aristidi et al. 2009). The Guiding camera is an SBIG ST402M ensuring, in normal observing conditions, a guiding stability of about 0.2 arcsec rms or better.

To ensure the proper functioning of the electronic components, the two compartments of the focal box were insulated using both cellular polystyrene plates (Depron™), which stem heat conduction, and reflective layers (Kapton™), to prevent heat radiation, and heated with electric resistors to maintain their surrounding at temperatures compatible with safe operations. PT 100 thermometer probes are used to give feedback on regulators. The first compartment is stabilized at around -40°C, while the second compartment is held at approximately -10°C. On the other hand, the Science camera front panel is held at $+5^\circ$C as our FLI mechanical iris shutter could not be robustly operated at lower temperatures. All the thermal controllers are linked via an RS 485 bus to the main control computer through an RS 485/RS 232 adapter. So, all component temperatures can be monitored, and the set points of the controllers adjusted by software.

The double-glazed optical window of the focal box, composed of the two first meniscus lenses of the Wynne field corrector, minimizes heat loss, and reduces turbulence in the optical path of the instrument (Guillot et al. 2015). Lenses of the Wynne field corrector are in fused silica in order to minimize their thermo-elastic deformations. Moreover, insulation of the focal box guarantees a long life of the dichroic coating when external temperature can reach -80°C in winter.

2.2 Control software

The telescope is driven by a custom-made software, designed to operate both in a manual and automatic mode of operation. In the latter mode, a custom script describing a set of independent observing fields feeds the software. Each field has its own observational constraints (priority, temporal boundaries, sun elevation, periodicity. etc.) so the software schedules its observation following these constraints. To ensure proper pointing of the telescope in the automatic mode, the software uses a built-in field recognition algorithm, developed by the team, capable of re-pointing the telescope even in the case where the telescope pointing error is larger than 1°.

ASTEP 400 is connected to a dedicated computing and mass storage server (48 CPUs, ∼20 TiB). Data are locally stored on to a data acquisition PC (2 TiB disc capacity) and backed up automatically, every day, on the mass storage. A second data backup is made on TiB-capacity hard drives and sent back to our laboratory in Nice during the summer campaign. A data backup hard drive set is kept on-site for security in the (rare) cases of disc failures or shipping problems. Since 2013, permanent Internet link, with a typical bandwidth of 256 KB s^{-1}, allows us to take control of the telescope at any time, from any location, either to change the observing programme or to update the control software. However, the bandwidth is not sufficient to enable data transfer.

2.3 Frosting and snow deposit

During Antarctic winter, the temperature, which can fall down to -80°C, is characterized by some rapid variations that can reach several degrees per hour. In such conditions, the relative humidity leads to ice nucleation and frost formation on the primary mirror of the telescope and, to a lesser extent, on the secondary one. Ice dust can also fall on the primary mirror of the telescope. There are two ways to prevent the frost formation and/or snow deposit: (i) blowing dry air (continuously or from time to time) on optical surfaces or (ii) warming them up. The first method is optically safer since it is not likely to introduce significant turbulence inside the telescope's tube. The second method is more efficient but may produce turbulent plumes inside the tube, if used incorrectly. However, if the temperature differences between the mirrors and the local atmosphere stay below a safety limit (e.g. ∼6°C and ∼2°C

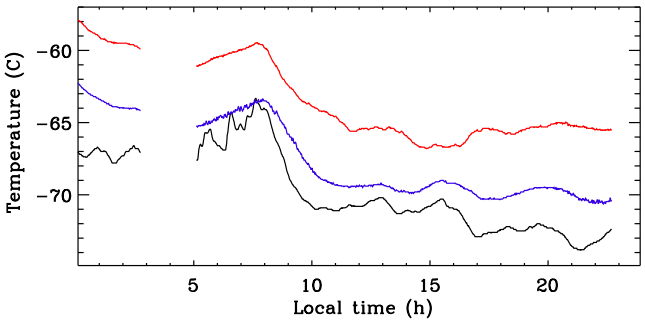

Figure 3. Ambient (black), primary (red) and secondary (blue) mirror temperatures as a function of local time on 2012 July 4. Typical temperature differences of the primary and secondary mirror are of ∼6°C and ∼2°C, respectively. Heating up the mirrors in this way, relative to the atmosphere, prevents frost formation on these mirrors.

for the primary and secondary mirrors, respectively), the effects on the image quality remain acceptable.

As no defrosting system was installed originally, daily human interventions were required, during the first year of operation of the instrument (2010), to check the status of the telescope mirrors and occasionally defrost the primary mirror and/or remove the ice dust deposit with a soft brush. To reduce these human interventions as much as possible, we have installed, during the second year of operation of the instrument (2011), a defrosting setup for both the primary and secondary mirrors. This system consists of a custom-designed film resistor attached to the rear surface of each mirror. Temperature probes were glued on the side of these mirrors, and a pair of additional temperature controllers were added to drive the heaters. These new controllers were connected to the same RS 485 bus as the other temperature controllers. So, the temperatures of the mirrors can be monitored easily, and the power supplied to the heaters adjusted to avoid any additional optical turbulence caused by this system. To evaluate the defrosting system efficiency, we analysed PSFs as a function of temperature gradients of the mirrors. We identified visually that alterations of the PSF quality remained small when the temperature difference (ΔT) between the primary and secondary mirrors and the ambient air remained lower than ∼10°C and ∼4°C, respectively. However, an a posteriori analysis of the data shows that the PSF size increases with the temperature difference, at a rate of 0.23 arcsec K^{-1} (Guillot et al. 2015).

This defrosting setup can operate both in 'preventive' or 'curative' mode. In the preventive mode, a small fraction of the maximum power is supplied to the heaters, so as to maintain the surface mirror temperature a few degrees above ambient temperature i.e. ∼6°C for the primary mirror, and ∼2°C for the secondary one (Fig. 3). This mode can run during observations without hampering the PSF quality. Under special weather conditions (rapid increase of the external temperature), some frost can appear in any case or, more frequently, ice dust grains can fall on the optics. Then, the curative mode is activated and 100 per cent of the nominal power of the heaters is supplied, for a short period, to remove the frost and the ice dust deposit. No science exposure frames are recorded during the defrosting curative phase.

3 OBSERVATIONS

ASTEP 400 was designed to achieve photometric accuracy of a fraction of millimagnitude over time-scales of few hours for bright ($R \sim 12$ mag) stars. These specifications make this instrument ideal for monitoring several thousands of stars to search for transiting exoplanets, and well suited for a variety of wide-field imaging and temporal studies, such as the discovery and monitoring of variable stars (Chapellier et al. 2016). ASTEP 400 is a semi-robotic and fully computer-controlled instrument, so that very few human interventions are required from the winter-over crew. Only regular inspections of the primary and secondary mirrors are needed. Through a single graphical user interface, the winter-over crew member in charge with ASTEP 400 can monitor the relevant parameters of the telescope, perform any modification, send orders to the telescope motor drives or run pre-determined observation scripts.

Table 1. Antarctic seasons and periods of various instrument operations.

'Summer' season	November–February
'Winter' season	March–October
Telescope installation	December 2009
Telescope operation	January 2010–December 2013
Telescope repatriation	February 2014
Telescope maintenance	November–December
Calibrations	December–March
Science observations	April–September
Data repatriation	February

Table 1 presents the characteristics of Antarctic observations and various operations of an instrument operating at Dome C. There are two distinct operational seasons for ASTEP 400 as for any optical instrument located at Dome C: (i) the summer season, from November up to the end of January, used for instrument maintenance and upgrading, including the installation of new instruments, and (ii) the winter season, from March to October, with transitional periods, February–March, used for calibrations, while waiting/preparing for astronomical darkness, and September–October at the end of the winter-over season, used for data backup and preparing for the next summer season (Table 1).

3.1 Duty cycle and technical issues

The winter clear sky fraction at Dome C was studied by several authors. Mosser & Aristidi (2007) yielded an estimate of 84 per cent of clear sky fraction by reporting, several times a day, the presence of clouds with the naked eye, Moore et al. (2008) derive a fraction of 79 per cent from the Gattini instrument while Crouzet et al. (2010) and Ashley et al. (2005) found a fraction of 74 per cent from the 2008 ASTEP South data and from the 2001 ICECAM images, respectively. Recently, Petenko et al. (2014) obtained a fraction of 60 per cent of completely clear sky conditions from sodar measurements.

The duty cycle for winter observations at Dome C was qualified by the ASTEP South instrument (Crouzet et al. 2010). The main limitations were related to (i) the position of the Sun, (ii) the weather conditions and (iii) technical issues that have prevented normal operation of the instrument. Influence of the Sun (and the Moon) on photometry at Dome C was also studied by Crouzet et al. (2010). It is important to notice that although the Sun is permanently below the horizon from May 6 to August 9, the sky background is always higher around noon preventing fully continuous photometric measurements. The *R*-band sky magnitude at Dome C is 16.6 mag $arcsec^{-2}$ for a Sun elevation of −9°, whilst the sky intensity drops to an undetectable level when the Sun is below −13° (Crouzet et al. 2010). In addition, an increased sky background is clearly seen during periods of full Moon. Therefore, special care has

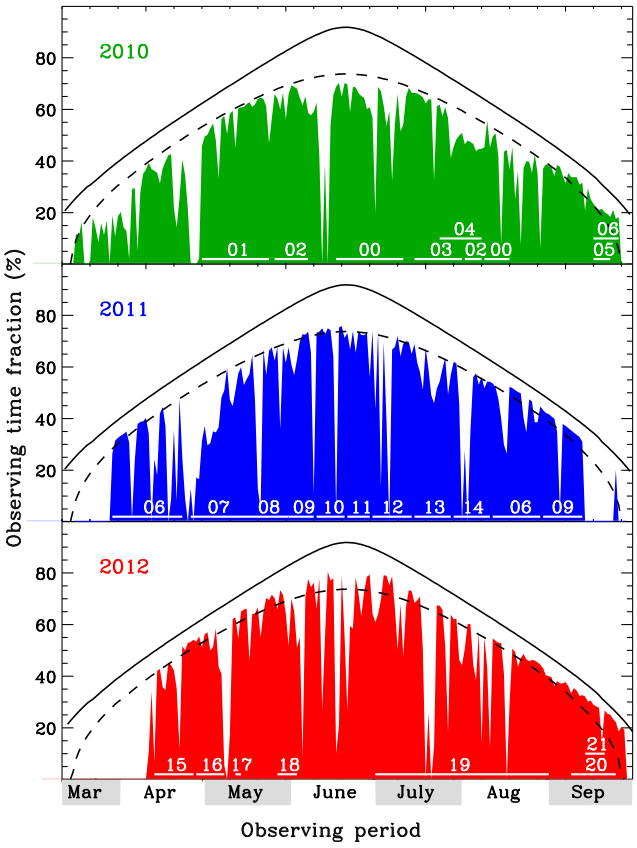

Figure 4. Daily observing time fraction for ASTEP 400 in 2010 (green), 2011 (blue) and 2012 (red) as a function of the observation period. The black solid line and dashed line indicate the fraction of time for which the Sun is lower than −9° and −13° below the horizon, respectively. Periods of observation of each field are superimposed on the corresponding plot.

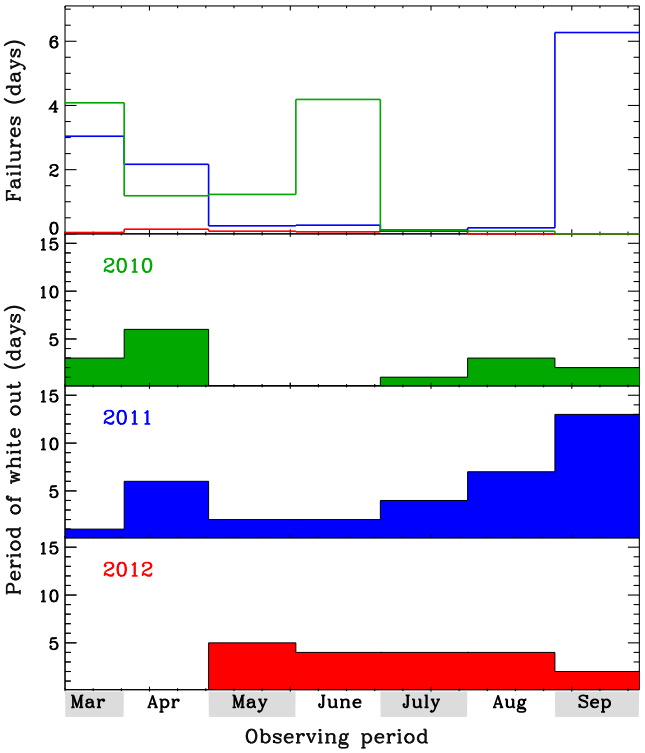

Figure 5. Monthly periods of whiteout observed at Concordia as a function of observing period in 2010 (green), 2011 (blue) and 2012 (red). The upper plot shows the period of unavailability of ASTEP-400 due to technical issues and maintenance operations of the instrument in 2010 (green), 2011 (blue) and 2012 (red). Details of the main issues are given in Table 2. Note that the 2011 September technical issue occurred during a period of whiteout.

to be taken in the choice of the observed fields during these periods. Aurorae were also feared to be a limit to the long-term photometry in Antarctica, but in any case our data were not contaminated by aurorae, confirming that their contribution to the sky brightness at Dome C is negligible, as suggested by Dempsey, Storey & Phillips (2005) and reported by Crouzet et al. (2010) from analysis of ASTEP South data.

Typically, ASTEP 400 scientific observations run from March up to the end of September for each campaign and data acquisition are performed automatically when the Sun elevation is lower than −9°. The duty cycle for the 2010–2012 campaigns of ASTEP 400 is represented in Fig. 4. The limit due to the Sun and the fraction of the science exposure observing time is shown for each day from March 12 to September 30. During this period, we acquired a total of 1959, 1889 and 1997 h of science exposure frames for the 2010, 2011 and 2012 campaign, respectively. This gives a duty cycle of 65.51 per cent, 63.15 per cent and 66.77 per cent if we compare each data acquisition duration to the maximum dark observing time (i.e. when the Sun is at 9° below the horizon), for 2010, 2011 and 2012, respectively. The main factors that limit the duty cycle are bad weather conditions and technical issues. Note that we started observing later in 2012, compared to previous years.

Fig. 5 shows the monthly periods during which no data have been acquired for the 2010–2012 campaigns, counting separately periods which are due to bad weather conditions (whiteout) from those related to technical issues and maintenance of the instrument. For our analysis, we consider that technical and weather events are independent, even if some technical issues occurred during periods of bad weather. Most maintenance operations were planned during periods when the sky is not dark enough (i.e. Sun elevation is greater than −9°) and/or during periods of poor atmospheric conditions. Periods of veiled sky and/or of poor guiding of the telescope mount, due to windy conditions, were not taken into account for this analysis. The main technical issues encountered were related to power cuts lasting for a few minutes to a few hours, mechanical adjustments of the telescope mount, particularly during the first year of operation of the instrument, some electronic component failures and, rarely, to perform some optical settings of the focal box. Fig. 5 shows that the weather conditions were better in 2010 and 2012 than in 2011. Whiteout periods of 15, 35 and 19 d were observed from March 12 to September 30, in 2010, 2011 and 2012, respectively. This corresponds to a fraction of 7.4 per cent, 17.2 per cent and 9.3 per cent of the total observing time. We had a total of 10.8, 12.2 and 0.45 d of various technical failures for 2010, 2011 and 2012, respectively. Table 2 gives details of typical issues that ASTEP 400 had to face with during the 2010–2012 campaigns. Note that the 6 d technical failures of September 2011, due to a breakdown of the data transfer device of the Science camera, occurred during a long period of whiteout. Fig. 5 also shows that technical issues and maintenance operations decreased in 2011, except for September 2011, and were negligible during the third year of operation of ASTEP 400. This is the direct result of the continuous improvement of the instrument during its two first years of operation.

Table 2. Main technical issues that occurred during the 2010–2012 campaigns.

Tech. Issue	March (days)	April (days)	May (days)	June (days)	July (days)	August (days)	September (days)
	2010 2011 2012	2010 2011 2012	2010 2011 2012	2010 2011 2012	2010 2011 2012	2010 2011 2012	2010 2011 2012
Mechanics	0.04 0.00 0.00	0.06 0.00 0.00	0.15 0.00 0.00	0.13 0.02 0.00	0.02 0.00 0.00	0.04 0.00 0.00	0.00 0.00 0.00
Computer	0.02 0.00 0.00	0.10 0.02 0.06	0.08 0.08 0.02	0.02 0.08 0.02	0.08 0.02 0.00	0.02 0.02 0.00	0.00 0.02 0.00
Power cuts	0.00 0.00 0.04	0.00 0.13 0.04	0.00 0.17 0.04	0.04 0.17 0.00	0.00 0.04 0.13	0.00 0.17 0.00	0.00 0.17 0.00
Electronics	0.02 0.04 0.00	0.02 0.02 0.04	0.00 0.02 0.00	0.00 0.00 0.00	0.00 0.02 0.00	0.02 0.00 0.00	0.00 6.08 0.00
Optics	4.00 3.00 0.00	1.00 2.00 0.00	1.00 0.00 0.00	4.00 0.00 0.00	0.00 0.00 0.00	0.00 0.00 0.00	0.00 0.00 0.00
Total (days)	4.08 3.04 0.04	1.19 2.17 0.15	1.23 0.25 0.08	4.19 0.27 0.06	0.10 0.08 0.03	0.08 0.19 0.00	0.00 6.27 0.00

From this analysis, we found that the average duty cycle for winter observations at Dome C, including bad weather and technical failures of the instrument, is 65.14 per cent. This result agrees well with that of Crouzet et al. (2010), obtained with ASTEP South. In addition, and as shown by Fruth et al. (2014), Dome C provides a significant advantage for transit search: within two weeks of observations, ASTEP 400 yields detection for planets at short periods that can only be achieved during a whole year from a temperate site.

3.2 Science observations

When the ASTEP programme was funded, in 2006, only a few transiting exoplanets were known. The ASTEP 400 observing strategy was then tailored towards the potential of an exoplanet transit survey from Antarctica on technical, logistical and scientific aspects, by observing, continuously, fields with a large number of stars. Using the CoRoTlux transit survey simulator, described in Fressin et al. (2007), we then estimated the number of new planet transit detections to about 10 to 15 for a 4 year operation of the instrument, depending on the red noise level. The main assumptions made by the model are the use of the Besançon model of the Galaxy to generate stellar populations (Robin et al. 2003), and by considering only massive planets (the mass of Saturn and more). Based on the statistically large *Kepler* exoplanets list, this expected number can be reduced to about 3 to 5.

ASTEP 400 has operated from 2010 to 2013, but only the first 3 years (2010–2012) were analysed. Near-continuous science observations were conducted from the end of March through the beginning of October for each year. During each Antarctic summer campaign and at the beginning of each Antarctic winter season, when the time is generally less favourable for science observations, due to the permanent daylight, we performed various calibrations of the instrument by monitoring some bright sources, using density filters (Table 1).

We observed a large number of scientific fields. Most of them were dedicated to the exoplanet transit searching programme, whereas a few others were dedicated to a follow-up microlensing observations programme in which we took part during the first year of operation of the instrument (Bachelet et al. 2012). We only focus here on the 22 stellar fields, observed as part of the exoplanet transit searching programme during the first 3 years of operation of the instrument, listed in Table 3, for which 209 313 'Science' frames were processed and 317 831 stars analysed.

These fields were selected by a star count method using the USNO CCD Astrograph Catalog3 (UCAC3). We focused our search on part of the sky that is permanently observable from Dome C (i.e. circumpolar). This part of the sky was divided into smaller fields of size 1 squared degree, which match the FoV of ASTEP 400. For each field, we retrieved the data from the UCAC3 catalogue and built colour–magnitude ($R - K$ *versus* R) diagrams to isolate and hence count the giant stars (RGB), from the red giant finger up to magnitude $R = 14$ mag where it is (normally) easily possible to discriminate between giants and other stars. Then with the use of two colour diagrams ($H - K$ *versus* $J - H$), we counted the number of upper main-sequence (UMS) stars (earlier than the spectral type A). With the help of the same diagram, we counted the number of very low main-sequence (VLMS) stars (late K and M dwarfs) that are visible in each field. The final selection of the observing fields was performed manually, looking at the characteristics of each field taking into account the following criteria:

(i) the fields do not have a large crowding; we preferred fields with more isolated stars to reduce problematic of contamination from background sources on the potential targets;
(ii) no bright stars ($R < 4$ mag) closer than 2° from the field centre in order to avoid diffused stray light;
(iii) low number of RGB and UMS stars;
(iv) large number of VLMS stars;
(v) avoid field with large variation of interstellar extinction.

Fig. 6 illustrates the location of the selected stellar fields dedicated to the exoplanet research programme, which we observed during the 2010–2012 period. A typical field, containing ∼10 000 stars at magnitudes up to $R = 18$ mag, was observed during ∼7 to ∼30 d, depending on observing conditions. During the first year of ASTEP 400 operation (2010), we observed, as a test of the instrument performances, two stellar fields centred on WASP-18b and WASP-19b, two well-known exoplanets. The primary goal of these observations was to retrieve their transit depths. The very high data quality allowed us to detect the secondary eclipse of WASP-19b after one month of continuous observations. It was the first detection of the secondary eclipse of an exoplanet in the visible from the ground. We derived an eclipse depth of 390 ± 190 ppm and inferred a brightness temperature of 2690^{+150}_{-200} K for the day-side of WASP-19b (Abe et al. 2013). Then, we resumed our initial observation programme (i.e. observing new stellar fields to search for new transiting exoplanet candidates).

4 DATA REDUCTION AND QUALITY

4.1 Data processing

Each frame produced by the FLI Proline camera is 32 MiB. A typical science observation 'night' produces 400 to 600 frames, including calibration frames. This corresponds to more than 12 GiB of data. We produced around 6 TiB of data per year. Since the Internet connection at Concordia is not sufficient for such a data flow, all

Table 3. Main ASTEP 400 stellar fields observed during the 2010–2012 campaigns.

Field	α (2000)	δ (2000)	Stars	Exp. time (s)	Date of observation start	Date of observation end	Frames	Duty cycle (%)[a]
F-00	01:37:25.00	−45:40:40.40	150	15	2010-06-17	2010-07-11	44 336	78
–	–	–	–	15	2010-08-09	2010-08-18	4484	29
F-01	09:53:56.00	−45:46:13.50	10 784	130	2010-04-30	2010-05-24	8067	79
F-02	15:56:18.70	−66:25:24.70	13 623	120	2010-05-26	2010-06-07	5891	87
–	–	–	–	70	2010-08-02	2010-08-08	1845	41
F-03[b]	15:54:48.40	−65:54:04.30	18 312	70	2010-07-15	2010-08-02	7864	57
–	–	–	–	100	2012-08-31	2012-09-28	3622	49
F-04[b]	15:46:11.00	−64:53:32.59	20 838	70	2010-07-24	2010-08-08	5396	50
F-05	15:43:50.79	−66:31:13.89	18 675	70	2010-09-17	2010-09-23	898	43
F-06	16:10:51.29	−66:21:25.10	14 011	70	2010-09-17	2010-09-26	3175	96
–	–	–	–	30	2011-03-29	2011-04-23	14 490	66
–	–	–	–	60	2011-08-12	2011-08-18	3503	77
–	–	–	–	90	2011-08-19	2011-08-29	3769	81
F-07	17:16:32.70	−55:30:04.59	16 748	120	2011-04-26	2011-05-02	262	9
–	–	–	–	60	2011-05-03	2011-05-14	5033	56
F-08	17:35:29.10	−55:45:47.09	12 892	60	2011-05-14	2011-05-31	10 957	72
F-09	17:36:16.00	−53:48:43.09	15 559	60	2011-05-31	2011-06-09	7699	82
–	–	–	–	120	2011-08-30	2011-09-04	1790	100
–	–	–	–	60	2011-09-08	2011-09-13	3146	100
F-10	17:20:37.00	−59:26:25.79	9845	60	2011-06-10	2011-06-20	9443	87
F-11	17:44:57.59	−58:21:16.60	9852	60	2011-06-21	2011-06-29	8495	95
F-12	17:35:19.89	−53:21:10.39	15 091	60	2011-06-30	2011-07-14	9443	67
F-13	17:48:03.40	−59:26:52.50	8190	60	2011-07-15	2011-07-28	9781	84
F-14	17:35:25.00	−57:51:23.10	9112	60	2011-07-29	2011-08-11	7556	74
F-15	17:21:51.00	−53:00:22.10	17 384	60	2012-04-12	2012-04-26	6928	77
F-16	17:12:14.10	−52:17:54.90	21 950	60	2012-04-27	2012-05-07	6805	88
F-17	17:07:31.39	−48:14:53.90	23 142	40	2012-05-11	2012-05-13	2210	80
F-18	16:23:09.30	−48:38:26.20	21 757	90	2012-05-26	2012-06-02	2563	44
F-19	23:34:50.59	−42:05:27.60	613	180	2012-06-30	2012-08-31	6819	33
F-20	16:24:16.29	−56:03:16.89	20 872	90	2012-09-08	2012-09-24	2193	12
F-21	16:28:35.09	−56:40:41.59	18 431	90	2012-09-13	2012-09-20	850	40

Notes. [a]Fraction of time of science data recording including systems overheads, compared to the fraction of time when the Sun is lower than −9°.
[b]F-03 and F-04 correspond to the fields Exo2 and Exo3 of Fruth et al. (2014), respectively.

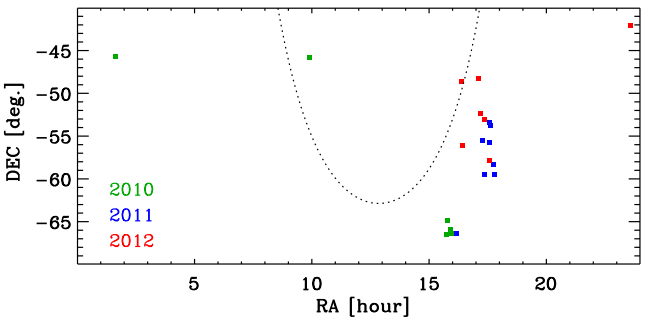

Figure 6. RA and Dec. positions of fields observed during the 2010 (green), 2011 (blue) and 2012 (red) campaigns. The dotted line represents the galactic plane. All observed fields are circumpolar. So they never rise nor set.

these data are transferred in Nice on hard discs at the end of each summer campaign. Thus, data from the winter campaign number n are available for full processing on February of year $n+1$.

The Science camera produces four types of frames: science, bias, dark and 'sky-flat' frames. As it is not easy to do twilight flats, nor dome flats, the photometric gain calibration is performed by using 'sky-flat' frames which are obtained by taking some science frames during periods when the sky background is high, i.e. when the Sun comes close to the horizon. After each of these sky-flat exposures, a slight random shift is applied to both the declination and right ascension axes of the telescope mount. The resulting flat frame is obtained by performing the median of all these individual exposures. By this way all stars, present on individual frames, are removed. Note that we had to deal with several optical diffusion additive effects including the so-called 'sky concentration' (Andersen, Freyhammer & Storm 1995). These additive effects were thus numerically fitted and subtracted on each frame.

The ASTEP 400 data process pipeline, only briefly described here (see Abe et al. 2013 for a complete description), exists under two different implementations: (i) a custom IDL code using classical aperture photometry routines from the well-known IDL astronomical library, and (ii) Miller–Buie implementation of the optimal image subtraction (OIS) algorithm (Miller, Pennypacker & White 2008). The first implementation is used for a daily on-site data processing at Concordia station, whilst the second, more computer time-consuming, is used after the data have been transferred back to France.

Each science exposure frame is bias subtracted, dark corrected, flat-fielded, and the astrometric solution is computed using reference stars from the UCAC4 catalogue. Aperture and OIS photometry are then performed. The OIS core algorithm is similar to the ISIS algorithm (Alard & Lupton 1998) that is known to be more

accurate than aperture photometry (Montalto et al. 2007). Indeed, we found that our OIS pipeline improves the scatter in all analysed light curves, compared to aperture photometry, by a factor of ∼1.5 in the rms noise, and makes the OIS data globally cleaner (Abe et al. 2013).

The OIS intrinsically removes global variations for all stars. For each field, we use a small number (typically 10) of reference stars, selected among more than 1000 stars, which do not present noticeable variations, to remove systematics. The selection criterion consists in keeping those stars that minimize the rms scatter of the normalized light curve. We have compared this calibration procedure with other methods such as SysRem (Tamuz, Mazeh & Zucker 2005), or the method described in Mazeh et al. (2009), without noticeable differences. Finally, we have applied a box-fitting algorithm (BLS: Box-fitting Least Squares; Kovács, Zucker & Mazeh 2002), to the calibrated light curves, to search for transits. Results presented here have been obtained with the OIS pipeline.

4.2 Characterization of ASTEP 400 noise

We follow closely the approach of Pont, Zucker & Queloz (2006) in estimating the level of correlated noise present in our data. We derive the photometric precision by looking at the remaining noise in each light curve, both point-to-point and on transit time-scale of 2.5 h, which is relevant for a hot Jupiter transiting a solar-like star. Binning, of course, will decrease the rms noise of the light curves and help to distinguish between the two noise components: (i) the random or white uncorrelated component, which is mainly a photon noise and (ii) the red or correlated component, caused by systematics, mainly atmospheric variations, observing conditions and telescope tracking. These parameters vary gradually over transit time-scales and add a red noise component to the white photon noise.

We compute the running average of each light curve over n points ($n = 50$) contained in a transit-length time interval of ∼2.5 h. Then we compare this curve to the rms scatter of the individual data point divided by the square root of the average number n of observations made in this transit-length time: $\sigma_w = \sigma/\sqrt{n}$, where σ is the standard rms noise of the whole light curve. For purely uncorrelated noise, these two sets of points should overlap. The amount by which the first set exceeds the second indicates the amplitude of the red noise over a transit-length time-scale.

Fig. 7 shows the light-curve rms noise *versus* ASTEP 400 R-band magnitude for stars of one of the 22 stellar fields (F-01), listed in Table 3, together with lines representing the theoretical photon noise, background noise, a 1 mmag systematics noise and the total noise budget limits. Light curves that show significant variability were removed before calculating the rms noise. From this plot, it is clear that we have obtained a photometric precision of ∼ 2 mmag for the brightest stars ($R \sim 12$ mag) of this field. For the dim end, the noise rises to ∼20 mmag at $R = 17$ mag. Although we achieve very high photometric precision for the brightest stars, it is evident that we are well above the photon noise limit. Fig. 7 also displays the rms noise of 50-consecutive-point averages compared to the expected scatter of the same data point averages in the presence of uncorrelated white noise. The dispersion of the mean of these 50 consecutive data points is much larger than $\sigma/\sqrt{50}$, showing that red noise dominates. The rms scatter in the binned data is ∼800 ppm for the brightest ($R \sim 12$ mag) non-variable stars, far worse than the ∼300 ppm that would be achieved if the noise was uncorrelated. Typically, for bright objects, the red noise causes the standard deviation to be ∼3 times larger than expected for uncorrelated noise,

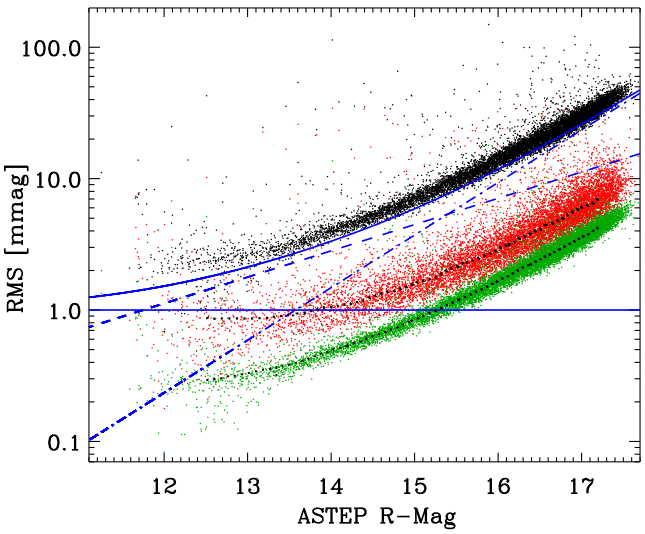

Figure 7. Typical photometric precision attained with ASTEP 400, as established from the point-to-point rms noise of the light curves after 3σ rejection of outlier points. Each point represents a light curve. Objects are those of one of the first stellar field (F-01), containing more than 10 000 stars, observed during the 2010 season. The upper group of symbols (black) shows the point-to-point rms of light curves for each star, the middle group (red) shows the rms noise of the same light curves after performing a moving weighted average over transit-length time intervals (2.5 h) and the lower group (green) shows the expected rms for uncorrelated noise (rms scatter of the individual data point divided by the square root of the average number n of points ($n = 50$) in a 2.5 h interval). The correlated noise amplitude among the brightest stars is ∼1 mmag. The blue dashed, dot–dashed, triple-dot–dashed and solid lines represent the source photon noise, sky photon noise, a 1 mmag constant added to account for systematics and the final expected precision (quadrature sum of the other three lines), respectively. The black dotted lines show the expected median rms noise for uncorrelated and white noise.

over transit-length time-scales. This analysis is rather similar for all fields.

Pont et al. (2006) show that the covariance structure of the correlated noise is quantified by the power-law dependence of the rms scatter in the binned data:

$$\sigma_n = \sigma\, n^b, \tag{1}$$

where σ_n is the rms scatter of the binned light curves. For totally uncorrelated noise, we expect $b = -0.5$, whereas $b = 0$ for fully correlated noise. We plot in Fig. 8 b as a function of ASTEP 400 R-band magnitude. As expected, effects of correlated noise are most pronounced for the brightest stars. However, even at our faint cut-off limit ($R \sim 18$ mag), we do not recover the uncorrelated noise value of $b = -0.5$.

We also examined the amount of correlated noise in our light curves using method of Smith et al. (2012). Fig. 9 displays the rms noise of the binned light curves as a function of bin width, for three stars of magnitude 13, 15 and 17, respectively, selected randomly amongst those which present no evident variations in their light curves in the field F-01. Fig. 9 shows that a large amount of correlated noise is present in our data at all time-scales. However, the rms noise seems to decrease less rapidly with the bin width for faint stars than for bright stars. This should be related to the fact that for faint stars the photon noise becomes larger than the red noise. Presence of correlated noise at all time-scales does not help to provide a clear understanding of its origin, which we further try to evaluate in various ways.

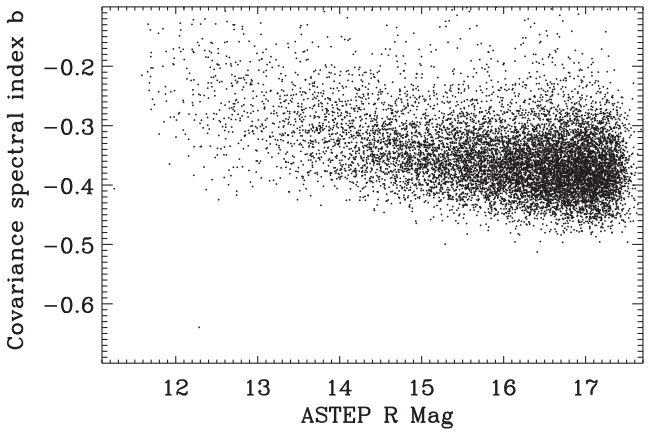

Figure 8. Covariance spectral index b as a function of ASTEP 400 R-band magnitude. Pure uncorrelated (white) noise should give $b = -0.5$, while pure correlated noise should give $b = 0$. We see that effects of correlated noise are more pronounced for the brightest stars of our field.

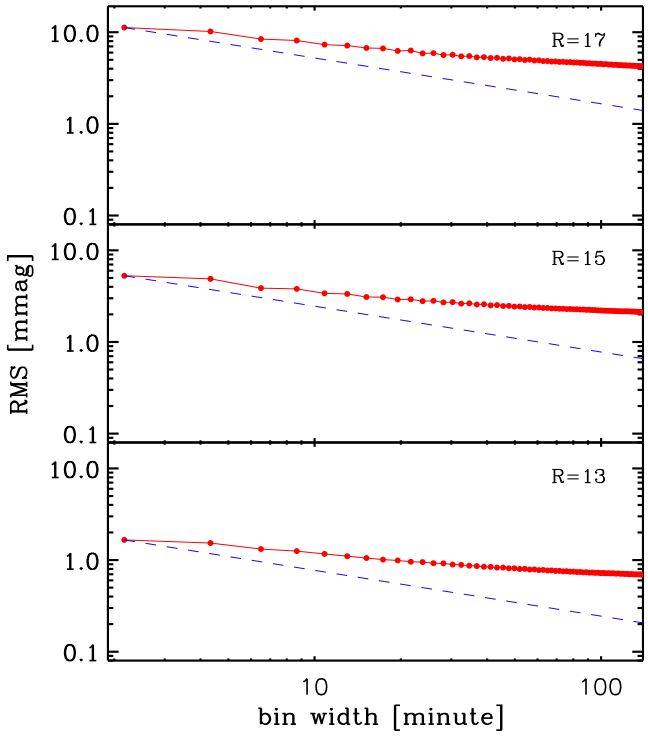

Figure 9. rms noise as a function of bin width of three random light curves, with star brightness decreasing from top to bottom. The blue dotted lines represent the rms noise versus bin width relation for an uncorrelated noise.

4.3 Origin of the correlated noise

Despite the decrease of systematic errors that affect our photometry by applying the trend-filtering algorithm (Kovács, Bakos & Noyes 2005), other effects, less easy to quantify, remain. For example, rapid temperature variations associated with telescope flexure could be the source of an asymmetrical deformation of the PSF causing astigmatism and de-collimation of the optical beam. The large ASTEP 400 spectrum band pass could introduce a significant colour-dependent terms into the atmospheric extinction correction, etc. In order to make a quantitative estimate of the remaining correlated noise in our light curves, we performed a search for

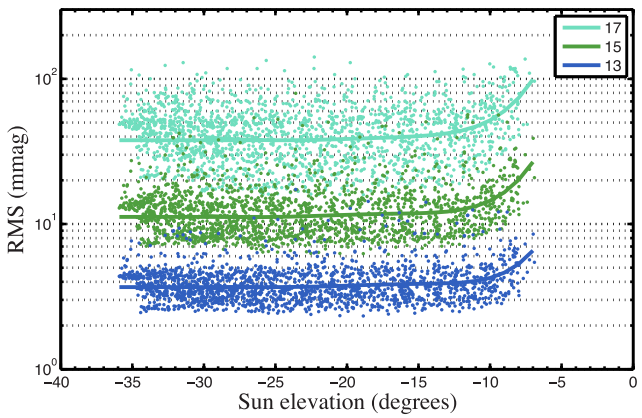

Figure 10. rms noise level as a function of the Sun elevation, for different star magnitudes between 13 and 17 (as labelled).

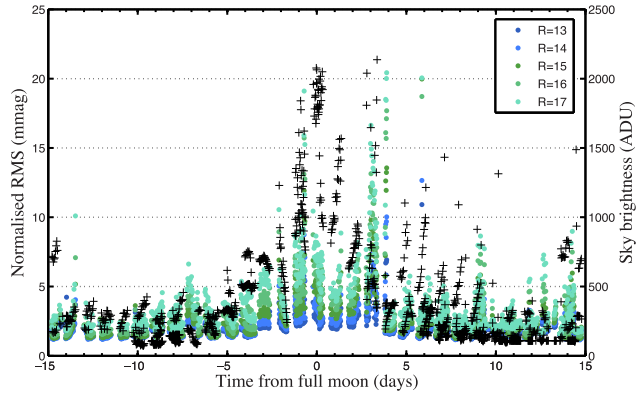

Figure 11. rms noise level as a function of the Moon phase for three different star R magnitudes (colour filled circles), as labelled, compared to the sky brightness as obtained from the background of the images (black crosses). Data have been folded with the synodic periodicity of the Moon. It shows an important increase of the sky background during the 2–3 d before and after the full Moon, depending on the distance of the field to the Moon. In order to compare the sensitivity of the photometric quality to the background brightness for the different magnitudes, the rms values have been normalized by the corresponding photon noise level, i.e. by multiplying the rms value by the factor $10^{-(R-12)/2.5}$.

correlations of the rms noise with a number of external parameters, including the sky level due to the Sun elevation or to the Moon, the image FWHM, the jitter of the stars on the chip and mirror defrosting temperature variations, etc.

4.3.1 Influence of the Sun and Moon

First, we examine in Fig. 10 how the elevation of the Sun influences the rms noise of the light curves. As Crouzet et al. (2010), we find that the light curves are not affected by the Sun as long as its elevation is less than -13° for $R = 17$ mag stars and -10° for $R = 12$ mag stars. This implies that, in principle, observations can be conducted with a maximum duty cycle of 70 per cent for faint stars and up to 90 per cent for bright stars at the winter solstice (see also Fig. 4).

The sky brightness also strongly depends on Moon phase and can be significantly higher than average (up to a factor of 10) around the full Moon (Fig. 11). This affects the photometric quality for stars fainter than $R = 15$ mag during 2 to 3 d before and after the

full Moon, depending on the distance of the Moon to the field. An increase of the noise level for stars brighter than $R = 14$ mag is present, but less significant. In summary, observing stars brighter than $R = 14$ mag is possible most of the time, while we should take into account the Moon phase and Sun elevation when observing faint stars. This effect could be minimized if we have sharper PSFs, as the contribution from the background would be lower.

4.3.2 *Astrometry and jitter noise*

Tracking defects and telescope mechanical jitter are also yield photometric noise. Ideally, tracking should have a sub-pixel accuracy for safe photometry. Special efforts have been done at the design level to make tracking as accurate as possible. A guiding camera, hoisted in the thermally controlled camera box, was in charge to real-time tracking corrections. To assess the efficiency of this system, we have selected a sample of 3885 frames taken in May 2011, on field F-08 (see Table 3).

For each frame, an astrometric reduction was performed using a local implementation of the 'astrometry.net' online astrometry service (http://astrometry.net; see Lang et al. 2010). The resulting World Coordinate System parameters, including fourth-order Simple Imaging Polynomials, leads to the J2000 coordinates of the central pixel, the on-sky field orientation and scale.

On the sample under study, the on-sky scale fluctuates between 0.9295 and 0.9297 arcsec pixel^{-1}. This slight fluctuation yields sub-pixel PSF motion in the corners of the image. The rotation angle has a sinusoidal time variation with an amplitude of 7 arcmin. This is a consequence of a polar misalignment of the telescope, due to both slight initial alignment defects and to long-term ice creeping. For pixels close to the corners of the image, this leads to PSF motions of ± 6 pixels. The central pixels move on the sky but stay within an error box of ± 2 pixels in declination and ± 7 pixels in right ascension. This is due to internal flexures that shift the guiding camera *w.r.t.* the science camera.

These astrometric defects (on-sky position jitter and field rotation) have been cross-correlated with photometric rms accuracy data, but no clear-cut correlation appears. These defects do not appear to be a relevant fraction of the photometric accuracy budget.

Position jitter would deserve to be corrected for the next generation of instruments. This would require extra engineering efforts to lower internal flexure and/or to incorporate software compensation. However, for the on-sky field rotation issue, the solution seems more difficult to implement. Indeed, the non-deterministic creeping of the ice sole on which the telescope is set will lead to long-term misalignment, even if the initial alignment was perfect (Crouzet et al. 2010). In addition, sub-arcminute initial alignment is a challenge in Antarctic conditions. This effect will affect more deeply wide-field imagers for transiting exoplanet discovery. However, narrower field instruments for known targets follow-up would be less affected by this residual field rotation.

4.3.3 *Snow and ice as sources of noise*

At Dome C, snowfall is rare. Its accumulation, which ranges from 25 to 32 mm water equivalent per year (Frezzotti et al. 2005), is due to precipitation, sublimation/deposition and wind-blown snow. Wind-driven sublimation processes, controlled by the surface slope in the wind direction, have a huge impact on snow precipitation. The surface snow is lifted by wind (when its speed exceeds about 6 ms^{-1}) and ice crystals remain often present in the atmosphere a few days after the decrease of the wind speed. Hence, under clear sky conditions, snow precipitation occurs as ice crystals often called *diamond dust*.

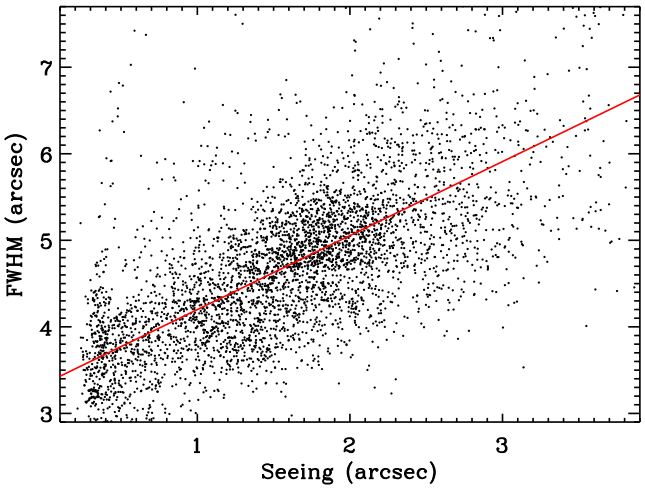

Figure 12. Correlation between the PSF FWHM and independent seeing measurements from the differential image motion installed close to the instrument at a height of 8 m. A linear regression gives a slope of 0.85 with a correlation coefficient of 0.65.

Outside whiteout periods, during which no observation is conducted, the wind-blown snow can also fall on the primary and secondary mirrors of the telescope during clear sky conditions creating a time-variable background. The defrosting system installed during the second year of operation of the instrument has been fairly successful to prevent the frost formation, but human interventions have been favoured for cleaning optics of the telescope after whiteout periods over using the defrosting curative mode which typically lasts a few hours, depending on the thickness of the ice deposit. We believe that the best way to prevent ice crystals deposit on the primary mirror is to install a dry air blower system under pressure that will send regular blows of air on the mirrors. We have found no significant reduction of the red noise between manual (human intervention) and automatic defrosting of the mirrors. We have always cleaned manually the telescope's optics after each whiteout period.

The focal box is perfectly sealed preventing ice crystals from entering the focal box. We did not see any frost formation nor snow deposit on the entrance of the focal box.

4.3.4 *FWHM versus seeing*

As discussed by Guillot et al. (2015), the ASTEP star images were significantly broader than the expected $\sim$2 arcsec FWHM that had been estimated as being optimal to minimize inter-pixel noise (Crouzet et al. 2007). Fig. 12 shows the mean FWHM of each image of the field F-01 as a function of the independent seeing measurements provided by the differential seeing monitor (a DIMM instrument; see *e.g.* Aristidi et al. 2009) installed close to ASTEP 400, but at a height of 8 m. The PSF FWHM is clearly affected by the seeing variations, with a linear correlation coefficient of 0.65. Importantly, the intercept of the fit is at 3.5 arcsec, consistent with the measurements of Guillot et al. (2015) during the summer campaign of 2013 and suggesting that the PSFs are broadened by other factors such as astigmatism, thermally induced defocus, beam de-collimation, turbulence on the optical path or mechanical jitters inducing PSF spreading. Indeed, although lot of care has been taken to optimize the mechanical/optical design of the instrument,

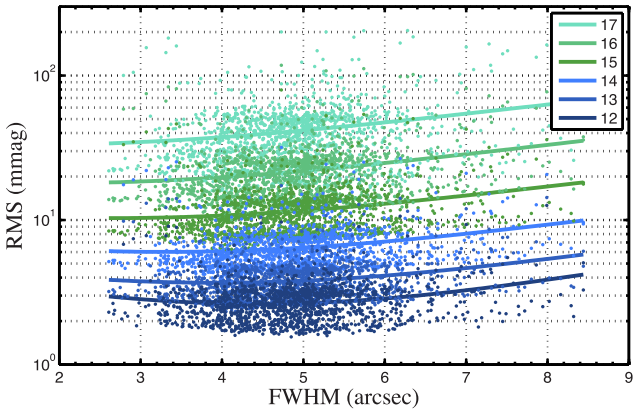

Figure 13. rms noise level as a function of the PSF FWHM for different star magnitudes. A degree-two polynomial fit has been applied to the data to put in evidence the different behaviour of the rms dependence to the FWHM for different magnitudes.

the atmospheric temperatures at Dome C can change so much and so rapidly that some mechanical slack had to be introduced in the driving motor gear to avoid jamming. For future observation campaigns in Antarctica, special effort should be done to address this issue.

The changes in instrumental settings and modus operandi prevented a finer analysis of the data, so that we could not identify the main source of the PSF broadening.

4.3.5 rms versus FWHM

Fig. 13 analyses how the standard deviation of the light curves depends on the value of the PSF FWHM. A quadratic fit for each magnitude shows that stars with different magnitudes behave differently. Bright stars ($R \sim 12$ mag) benefit from slightly larger values of the FWHM around 4 arcsec, whereas faint stars ($R \gtrsim 14$ mag) see their signal always degraded when the FWHM increases. It has to be noticed that no special care was applied on observing bright stars, as the experiment goal was to observe as many stars as possible, so stars brighter than $R = 13$ mag could saturate at some moment during the observations. Moreover, the OIS data processing is certainly not optimized for bright stars, as the remaining difference between the fitted PSF and the actual one could still be important, when it will be smaller than the background for fainter stars. The most important feature that can be seen here is the increase of the noise level with FWHM for faint stars (about a factor of 2 between 3 and 7 arcsec FWHM for an $R = 16$ mag star, in average). It is most certainly due to the contamination of the light curves by sky background and background stars in crowded fields. This can help understand why ASTEP got less good results than the comparative mid-latitude survey BEST for faint stars while doing much better at the bright end of the spectrum (Fruth et al. 2014). Having sharper, more regular and more stable PSF would give much precise photometry for any type of stars.

4.3.6 rms versus telescope orientation and airmass

The analysis of the variations of the light-curve rms as a function of telescope orientation (hour angle, elevation) should, in principle, allow us to determine whether the measured red noise is due to instrumental effects such as flexions of the telescope, an optical misalignment or heating-generated turbulence on the optical path.

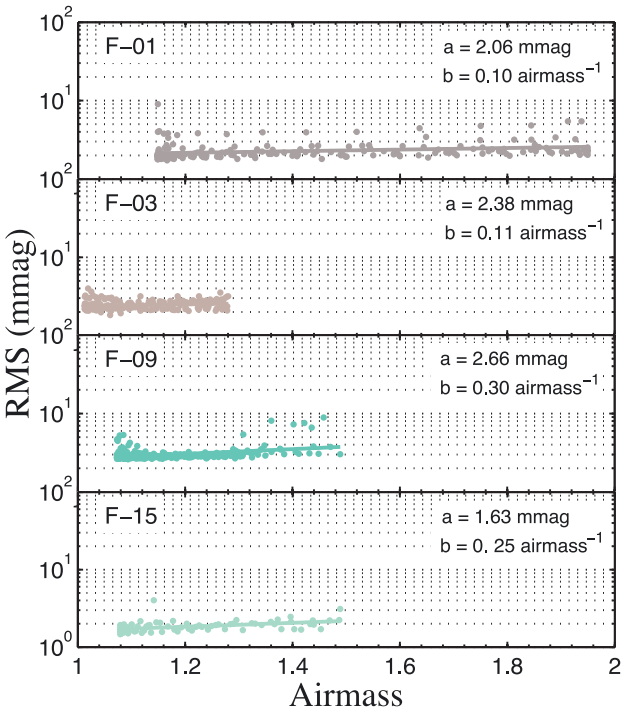

Figure 14. rms per minute in mmag for $R = 13$ mag stars as a function of airmass for four pointings (see Table 3). Linear fits are indicated, with a being the intersect in mmag and b being the relative slope in airmass^{-1} (see equation 2).

The variations in behaviour of the light curves as a function of each parameter, from one field to the next, are significant. This prevents a global analysis that would be independent of other factors.

We present in Fig. 14 examples of how the rms of bright stars varies as a function of airmass for four different fields. In order to do so, we selected the rms relations obtained for $R = 13$ mag stars and filtered out the points obtained when the sky brightness was larger than 500 ADU or FWHM values above 7.5 arcsec. We fit the rms–airmass relation as follows:

$$\mathrm{rms} = a\ 10^{b(\mathrm{airmass}\ -\ 1)}. \qquad (2)$$

This relation varies strongly from one field to the next, and a similar situation is observed when plotting as a function of elevation or hour angle. Typically, we observe a slope b in airmass^{-1} that is as low as 0.1 in good cases and as high as 0.3 in bad cases. The lowest values of b are found for observations during the first year, in 2010, and are always higher for later observations. Atmospheric contributions alone, as scintillation and extinction, cannot explain these slope values, even in 2010.

Scintillation is known to be very low at Dome C. This remains true even in the case of a bad seeing, because scintillation is due to a high-altitude turbulent layer, whereas the seeing measured at the ground level mainly comes from a thin surface layer that does not contribute to the scintillation noise. On-site measurements show that scintillation is responsible for an rms variation that is of the order of 0.1 mmag at zenith and rises strongly with airmass but is only of the order of 0.5 mmag at airmass 2 (Kenyon et al. 2006; Trinquet et al. 2008), independently of the star magnitude. This is much lower than the variations seen in Fig. 14, especially when considering that the trends that we see for $R = 13$ mag remain very similar even at $R = 17$ mag for which scintillation is negligible.

The typical atmospheric extinction in the visible at Dome C is around 0.1 mag airmass^{-1} (Vernin, personal communication). This decrease in flux yields a corresponding increase in rms of 5 per cent airmass^{-1}, or a slope corresponding to a value of b of 0.02 airmass^{-1}. Again, this is much smaller (by around one order of magnitude) than the variations seen in Fig. 14.

We would expect the increasing airmass to yield a corresponding increase in PSF size, as the seeing contribution increases with the airmass. Because, as seen previously, a larger PSF generally yields an rms increase, this may explain part of the trend seen in rms/airmass. Surprisingly, we could not any significant correlation between airmass and PSF size in individual fields whereas a weak increase was seen when considering all stars independently. It has to be noticed that the dispersion in PSF size is large, therefore possibly preventing such a fine analysis.

Altogether, the rms/airmass trend appears to be instrumental. It could be due to turbulence on the FoV, as advocated in Guillot et al. (2015), but the lack of a corresponding variation of the PSF sizes implies that this is more complex than a simple increase of instrumental seeing. Another possibility is that this is due to optical and/or mechanical imperfections. The fact that situation has slightly deteriorated over the years may point to a progressive misalignment of the telescope. Deformations of the telescope under its own weight as a function of pointing may also play a role.

4.3.7 Discussion

Although we cannot identify with certainty the sources of red noise in our data, our analysis provides some hints and guidance for future improvements. One feature in the data is that the PSFs are very broad. This is not necessarily a disadvantage for bright, isolated stars, but we have seen that it becomes one for faint stars, especially in crowded fields. As discussed by Guillot et al. (2015), this comes from a combination of instrument seeing due to thermal gradients across the line of sight and poor seeing on the ground. The depth of the ground layer at Dome C is lower than 5 m 17 per cent of the time but it is between 5 and 20 m 38 per cent of time and for the 45 per cent remaining, it is thicker than 20 m (Aristidi et al. 2009; Petenko et al. 2014).

We have seen that the weather at Dome C is generally very good, but the Moon is a significant disrupter of the photometry about 25 per cent of the time. Another difficulty that we experienced with ASTEP 400, and is characteristic of wide-field surveys on ice, is that the telescope alignment tends to slowly move during the season (Crouzet et al. 2010), implying that stars on the border of the CCD cannot be maintained on the same pixel. This can contribute to the red noise as well. Finally, a correlation with elevation was found and remains unexplained. This may be due to mechanical effects, convective plumes moving on the line of sight or a combination of effects.

We identify several improvements that would readily improve the PSF quality and should increase the photometric accuracy of the instrument. Ventilating the mirrors and thermal box window with a laminar flow of dry air would minimize density fluctuations on the optical path and prevent frost deposits. The focal plane should be adjusted in real time in order to avoid defocusing. The telescope should be installed on a higher ground to minimize the contribution of atmospheric seeing. Finally, a tip-tilt system could be installed relatively easily and would take advantage of the slowness of the turbulence at Concordia. Already, the observations of WASP-19b (Abe et al. 2013) have demonstrated that even over long periods, an excellent photometric quality is within reach of Antarctic observations.

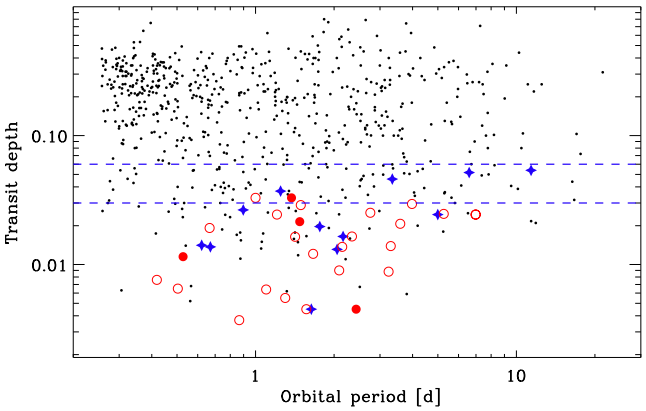

Figure 15. Transit depth versus orbital period for all systems that present transit-like features in their light curves. Black dots represent eclipsing binaries, red filled circles are our good planetary candidates, blue stars are candidates identified as eclipsing binaries and red open circles are unsettled candidates. The dashed blue lines represent our transit depth thresholds of 3 per cent and 5 per cent used as candidate selection criteria.

4.4 Comparison to other sites

Fruth et al. (2014) compared joint observations of the well-known exoplanet WASP-18b and of two target fields from Antarctica with ASTEP 400 and from Chile with BEST II, a 25 cm telescope, with a particular attention paid to the photometric precision and to the observational phase coverage. The photometric systems of the two instruments are expected to be similar, both instruments using the same CCD chip and both observing in a similar wide spectral band. To get a quantitative comparison based on a thorough assessment of the photometric noise budget obtained from each site, Fruth et al. (2014) used an analytical model of the photometric noise that includes contributions of a systematic red noise, a photon shot noise and a background noise, to fit the standard deviation *versus* magnitude plots of ASTEP 400 and BEST II light curves. For bright stars, the systematic red noise is dominant, while the background noise dominates for faint stars. Fruth et al. (2014) showed that for bright targets (e.g. WASP-18b) ASTEP 400 data present a smaller noise level compared to BEST II. However, the difference is not of the order of a factor of 2–4, as it would be expected given the sizes of the two telescopes and the smaller scintillation noise at Dome C. This indicates that systematic effects contribute significantly to the noise budget of ASTEP 400. On the other hand, the background noise has been found slightly higher for ASTEP 400, as compared with BEST II, for faint stars. This can be explained by the width and variability of the PSF, as found in a detailed analysis (Guillot et al. 2015). However, as far as transit detection efficiency is concerned, the high duty cycle of observations from Dome C gives a decisive advantage to ASTEP 400.

5 TRANSIT CANDIDATES

5.1 Transit search

To search for possible planetary transits, we performed a BLS period search (Kovács et al. 2002) on light curves of each stellar field, using BLS with trapezoidal signal fitting. BLS allows fast and efficient search for transits and provides rank-ordered lists of the best light

Table 4. List of selected ASTEP 400 exoplanet transit candidates.

Cand.	ASTEP-ID	UCAC4-ID	α (J2000)	δ (J2000)	*V* Mag	*R* Mag	*J* Mag	*H* Mag	*K* Mag	Field
C-1	A-031-1432-1080	U4-117-120529	16:12:28.31	−66:36:02.62	12.25	12.17	11.16	10.93	10.86	F-06
C-2	A-009-0788-3195	U4-223-043932	09:55:20.07	−45:25:11.28	14.13	14.48	13.11	12.84	12.73	F-01
C-3	A-009-3827-0876	U4-220-040923	09:50:53.41	−46:00:56.56	16.50	16.21	15.54	15.12	15.10	F-01
C-4	A-009-2480-1645	U4-221-041868	09:52:51.83	−45:49:12.82	16.20	15.19	14.84	14.19	14.11	F-01
C-5	A-020-0766-3182	U4-122-142653	15:57:59.21	−65:36:10.80	15.13	14.92	13.46	12.79	12.63	F-03
C-6	A-020-3351-3239	U4-123-150641	15:51:34.43	−65:35:29.20	13.91	–	13.40	13.00	12.86	F-03
C-7	A-012-2686-3723	U4-121-140615	15:54:39.52	−65:59:38.19	14.55	15.56	14.30	14.01	13.87	F-02/F-03
C-8	A-012-2616-1638	U4-118-126574	15:54:48.84	−66:31:44.36	13.63	14.03	13.54	13.32	13.23	F-02
C-9	A-042-1493-1784	U4-181-196452	17:37:14.85	−53:52:32.07	17.01	13.59	11.97	11.54	11.40	F-09
C-10	A-040-3806-1347	U4-171-187216	17:32:16.60	−55:56:29.04	15.88	15.88	14.20	13.66	13.52	F-08
C-11	A-042-1344-1819	U4-181-196513	17:37:30.46	−53:51:57.75	12.50	12.54	11.35	11.14	11.08	F-09
C-12	A-009-3640-2734	U4-223-042828	09:51:10.06	−45:32:26.09	14.43	14.08	12.58	11.95	11.79	F-01
C-13	A-009-2138-2068	U4-222-041279	09:53:22.08	−45:42:40.05	16.06	16.01	15.23	15.01	14.85	F-01
C-14	A-037-2105-3878	U4-175-188215	17:16:24.97	−55:01:43.88	14.57	14.88	13.53	13.10	13.06	F-07
C-15	A-045-2152-2821	U4-185-192986	17:35:08.89	−53:09:03.27	13.03	13.06	12.05	11.76	11.72	F-12
C-16	A-012-3270-0293	U4-116-118563	15:53:06.94	−66:52:15.09	13.81	14.54	13.53	13.17	13.10	F-02
C-17	A-037-3129-2829	U4-174-179953	17:14:34.75	−55:17:53.55	13.54	–	12.88	12.55	12.45	F-07
C-18	A-045-3805-0481	U4-182-189991	17:32:18.77	−53:44:58.34	15.77	15.48	14.58	14.22	14.10	F-12
C-19	A-021-2548-0316	U4-124-144094	15:44:59.38	−65:19:55.89	15.22	13.32	13.37	12.87	12.80	F-04
C-20	A-021-2298-0771	U4-124-144273	15:45:35.97	−65:12:59.86	13.22	12.96	12.53	12.28	12.28	F-04
C-21	A-021-1387-1097	U4-125-146829	15:47:49.64	−65:07:55.28	14.39	14.24	13.64	13.38	13.27	F-04
C-22	A-042-0935-3675	U4-184-191506	17:38:09.96	−53:23:21.14	14.55	14.62	13.32	12.78	12.78	F-09/F-12
C-23	A-042-3059-3753	U4-184-190549	17:34:31.17	−53:22:21.86	15.57	14.98	14.43	14.08	14.01	F-09/F-12
C-24	A-053-2846-0663	U4-187-172292	17:10:56.16	−52:39:24.58	13.37	13.60	12.44	12.03	11.94	F-16
C-25	A-053-2656-1277	U4-188-174569	17:11:15.16	−52:29:59.70	14.00	–	13.14	12.57	12.29	F-16
C-26	A-053-1172-1642	U4-188-175770	17:13:45.37	−52:24:14.91	13.29	13.33	12.68	12.41	12.35	F-16
C-27	A-054-3685-2190	U4-209-133083	17:05:02.53	−48:12:51.69	12.99	13.07	11.71	11.48	11.42	F-17
C-28	A-055-3107-3596	U4-209-116230	16:21:32.53	−48:14:51.00	14.01	13.93	12.47	12.05	11.92	F-18
C-29	A-055-2846-1800	U4-207-115393	16:21:56.19	−48:42:28.07	15.09	14.11	13.33	12.86	12.69	F-18
C-30	A-055-2093-0212	U4-205-119263	16:23:07.26	−49:06:49.58	15.73	14.62	12.23	11.46	11.24	F-18
C-31	A-055-1859-0987	U4-206-118241	16:23:28.95	−48:54:58.29	13.73	12.89	12.36	11.87	11.77	F-18
C-32	A-055-0363-0217	U4-205-120592	16:25:48.56	−49:06:20.13	14.49	14.39	14.03	13.64	13.58	F-18
C-33	A-055-3499-1964	U4-207-114982	16:20:55.46	−48:39:55.04	13.19	12.36	9.47	8.60	8.31	F-18
C-34	A-055-2130-3575	U4-209-116840	16:23:02.74	−48:15:05.86	14.58	14.22	12.62	12.20	12.08	F-18
C-35	A-055-1859-1579	U4-207-116242	16:23:28.65	−48:45:50.26	14.47	14.14	13.65	13.31	13.17	F-18
C-36	A-055-3989-2702	U4-208-120345	16:20:10.90	−48:28:32.88	15.93	15.24	12.23	11.31	10.83	F-18
C-37	A-055-1449-2398	U4-208-122291	16:24:06.66	−48:33:08.73	14.90	14.60	13.60	13.38	13.22	F-18
C-38	A-055-1334-1279	U4-206-118679	16:24:18.06	−48:50:25.41	–	14.48	13.06	12.72	12.53	F-18
C-39	A-055-1429-3231	U4-209-117316	16:24:07.81	−48:20:19.17	15.39	13.94	12.26	11.52	11.32	F-18
C-40	A-055-3438-0492	U4-205-118143	16:21:01.32	−49:02:28.89	14.44	13.94	12.29	11.83	11.68	F-18
C-41	A-055-0903-3693	U4-209-117629	16:24:55.67	−48:13:14.95	14.89	14.46	13.43	13.07	12.87	F-18
C-42	A-055-3244-1770	U4-207-115121	16:21:19.08	−48:42:54.87	14.91	14.36	12.32	11.60	11.40	F-18
C-43	A-055-3403-3609	U4-209-116070	16:21:05.45	−48:14:40.69	15.12	15.00	13.08	12.56	12.39	F-18

Note. Units of right ascension are hours, minutes and seconds, and units of declination are degrees, arcminutes and arcseconds.

curves based on their signal-to-noise ratio (SNR). We used OIS data for the whole analysis. We have first selected systems that present transit-like features in their folded light curves, with a transit depth smaller than 3 per cent. We rejected stars with a close (<3 arcsec) brighter companion and systems that show bad SNR and unusual variations in their light curves or other systematic problems. We then visually inspected systems with a transit depth of between 3 per cent and 6 per cent and selected six systems that present transit shape compatible with a planetary transit (Fig. 15). We did not adapt our depth criterion to the colour of the star and then probably reject a possible good M dwarf candidates.

From this analysis, we selected 43 transit candidates. We found also more than 1100 variable stars and 600 eclipsing binaries (EcBs) including all rejected planetary candidates that will be presented in a forthcoming paper (Chapellier et al. 2016). The 43 transit candidates are listed in Table 4. For each case, this table indicates the ASTEP 400 and UCAC4 identifications, coordinates, *V*, *R* magnitudes (from UCAC4), *J*, *H*, *K* magnitudes (from 2MASS) and the corresponding observed field. Fig. 16 shows the *R* Mag versus orbital period of all systems that present transit-like features in their light curves including our candidates. Note that the fraction of candidates in F-18 is higher than other fields. It is probably due to the fact that this field is quite dense with more than 21 000 stars and was observed during more than one month.

For each candidate, a transit model was fitted to the data. We used the publicly available Markov chain Monte Carlo (MCMC) suite EXOFAST (Eastman, Gaudi & Agol 2013) and the Transit Analysis Package presented by Gazak et al. (2012) to perform a fit of each transit light curve using the light-curve models of Mandel & Agol (2002). For each fit, we used priors on the orbital period, which

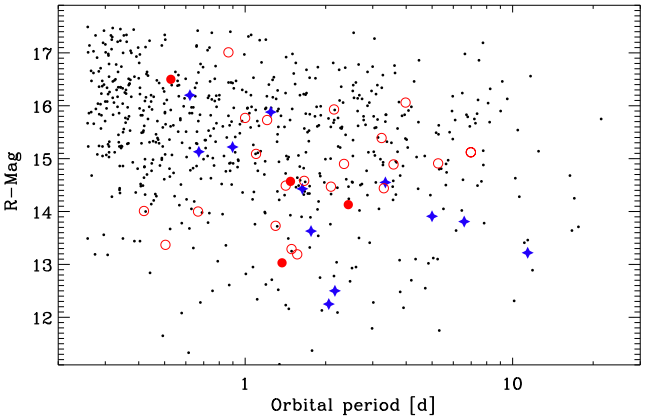

Figure 16. *R* Mag versus orbital period for all systems that present transit-like features in their light curves. Black dots represent EcBs, blue stars are candidates identified as non-planetary systems, red open circles are unsettled candidates and red filled circles are our good planetary candidates.

corresponds to the large BLS peak, and the epoch of the detected event as well as priors on the stellar effective temperature, gravity and metallicity when available.

The model fits for the ratio of planet to star radii ($r_p/R_\star$), the semi-major axis ($a/R_\star$) in units of stellar radii and the inclination of the orbit. In addition, EXOFAST fits for the stellar mass (M_*), the stellar radius (R_*), the planet radius (r_p), the temperature equilibrium of the planet (T_{eq}) and the impact parameter (b). We used the independent stellar densities ρ_t and ρ_{JK} calculated from transit parameters and $J-K$ colours, respectively, to identify the most promising transiting exoplanet candidates, as described in Tingley, Bonomo & Deeg (2011). We note that more definitive validation of planet candidates should involve the use of more elaborate tools using Bayesian statistics and known information on the population of stars and planets (e.g. Collier Cameron et al. 2007; Santerne et al. 2015). We leave this for future work.

5.2 Follow-up observations

Radial velocity (RV) follow-up is needed to identify the nature of the transiting object and establish the mass of the planet and the eccentricity of its orbit. This can be done by measuring the RV variation, which is directly linked to the mass ratio of the main star to its companion. We used the Wide Field Spectrograph (WiFeS; Dopita et al. 2007, 2010) on the Australian National University (ANU) 2.3 m telescope at Siding Spring Observatory and the High Accuracy Radial velocity Planet Searcher (HARPS) spectrograph, mounted full time on the 3.6 m telescope in La Silla, ESO, Chile, to perform spectroscopic observations for the brightest 2010 and 2011 candidates (Rupprecht et al. 2004). 20 of the 43 exoplanetary transit candidates were only observed as 2012 candidates were not yet processed when spectroscopic follow-up observations have been carried out.

For candidates observed with WiFeS, our strategy was to first take a low-resolution ($R = 3\,000$) flux-calibrated spectrum for spectral typing, to vet for false-positive scenarios involving giants. We then take multi-epoch $R = 7000$ RV measurements, timed at phase quadrature, to check for velocity variations at the km s^{-1} level that would point to the candidate being an EcB. The full reduction procedure is detailed in Bayliss et al. (2013). Since WiFeS is an integral field spectrograph with 38 arcsec × 11 arcsec FoV, spectra for nearby companions to the candidates are also extracted and analysed in the same way. There are instances where we find contamination from a nearby EcB to be the cause of the photometric signal. We match each observed flux-calibrated spectrum against a grid of synthetic spectra from the Munari library, fitting for T_{eff}, log g and [Fe/H] (Munari et al. 2005). For each grid point, the rms of fit is calculated. We preferentially weight log g sensitive regions (e.g., Balmer jump for hotter stars, Mgb and MgH regions for cooler stars) during the grid fitting, so that we can confidently differentiate between dwarfs and giants. We also account for interstellar extinction by iterating the fit over the possible reddening values up to the Schlegel maximum for the region (Schlegel, Finkbeiner & Davis 1998).

HARPS was used with the observing mode obj AB, without simultaneous thorium in order to monitor the Moon background light on the second fibre. The exposure time was set in between 30 and 45 min. We reduced the HARPS data and computed the RVs with the pipeline based on the cross-correlation techniques (Baranne et al. 1996; Pepe et al. 2002). RVs were obtained by weighted cross-correlation with a numerical G2 mask.

6 PROPERTIES OF CANDIDATES

Tables 5 and 6 summarize the transit parameters, i.e. orbital period, epoch of the transit, ratio of planet to star radii ($r_p/R_\star$), semi-major axis in stellar radii ($a/R_\star$), inclination of the orbit, number of the detected events and estimate of the stellar density ratio (ρ_t/ρ_{JK}) (where ρ_t and ρ_{JK} are the stellar densities calculated from the transit parameters and $J-K$ colour, respectively), for the 43 planetary candidates as well as the stellar parameters of the parent stars of candidates that have been followed up, including the effective temperature (T_{eff}), the gravity (log g), the metallicity ([Fe/H]), the stellar mass and radius, the planet radius, the semi-major axis and the equilibrium planet temperature derived from EXOFAST analysis.

On the basis of these observations, it was possible to conclude that (i) four of the candidates are found as good planetary candidates, and pending future more accurate well-sampled RV observations are required to confirm their planetary nature and to perform their complete characterization; (ii) 15 of the candidates were identified as non-planetary systems. These include spectroscopic binaries, background EcBs and blended binary systems. Candidates for which spectroscopic measurements have not been performed were classified as unsettled cases. From this list, 9 candidates were classified as unsettled good candidates pending future detailed investigations to confirm their probable planetary nature, while 15 candidates were found as unsettled non-planetary candidates or suspected binaries, according to the analysis of their transit parameters and their stellar density ratios, only. Note that five candidates are listed as mono-transits, as only a single transit event is present in their light curves.

Here we focus only on the four good transit candidates giving a brief overview over the properties of the parent star and the detected transit signal of each candidate. Any follow-up observations that have been performed are also described. The resulting catalogue of all candidates is made available online at http://astep-vo.oca.eu. We also make available the detrended light curves and RV measurements, when available, for all candidates.

C-2 (A-009-0788-3195, UCAC4 223-043932) is located in the field F-01. This relatively bright star ($V = 14.1$ mag) has a 0.49 per cent deep transit occurring every 2.4300 d for duration of 2.088 h. We detected a total of six transits for this system (Fig. 17). There is no bright source (up to $V = 16$ mag) close to this candidate, the closest star UCAC4 223-043929 being located at more than 6 arcsec, and blending can be ruled out. From ANU spectroscopic

Table 5. Transit parameters of ASTEP 400 planet candidates.

Cand.	Period (d)	T_C ($BJD_{TDB} - 2455000$)	$r_p/R_\star$	$a/R_\star$	i (degrees)	ρ_t/ρ_{JK}	Transit events	Status[a]
C-1	2.0545 ± 0.0001	458.1410 ± 0.0005	0.122 ± 0.005	7.4 ± 2.0	83.1 ± 2.0	0.25	3	2
C-2	2.4300 ± 0.0001	318.2246 ± 0.0005	0.070 ± 0.005	7.2 ± 1.0	84.6 ± 2.0	0.26	6	1
C-3	1.0548 ± 0.0001	318.2412 ± 0.0005	0.232 ± 0.005	2.4 ± 0.2	56.7 ± 1.0	0.24	12	1
C-4	0.6215 ± 0.0001	318.3609 ± 0.0005	0.117 ± 0.005	1.6 ± 0.2	45.9 ± 8.0	0.07	24	2
C-5	0.6700 ± 0.0780	392.2997 ± 0.0005	0.119 ± 0.005	1.7 ± 0.1	34.8 ± 6.0	0.07	14	2
C-6	4.9962 ± 0.0001	393.9094 ± 0.0005	0.160 ± 0.005	10.5 ± 0.5	85.4 ± 0.5	0.46	4	2
C-7	3.3440 ± 0.0001	397.9354 ± 0.0005	0.214 ± 0.005	9.4 ± 0.1	86.1 ± 0.5	0.48	3	2
C-8	1.7632 ± 0.0001	342.8838 ± 0.0005	0.148 ± 0.003	3.0 ± 0.1	83.3 ± 7.0	1.10	9	2
C-9	0.8659 ± 0.0001	713.2482 ± 0.0004	0.256 ± 0.005	2.4 ± 0.5	77.3 ± 5.0	0.64	16	3a
C-10	1.2473 ± 0.0001	696.8867 ± 0.0004	0.188 ± 0.004	3.1 ± 0.2	61.5 ± 5.0	0.97	7	2
C-11	2.1655 ± 0.0001	714.3793 ± 0.0005	0.118 ± 0.005	6.9 ± 0.5	84.5 ± 5.0	0.16	5	2
C-12	3.2720 ± 0.0001	318.3592 ± 0.0040	0.069 ± 0.005	2.0 ± 0.2	44.2 ± 9.0	0.01	8	2
C-13	3.9790 ± 0.0001	319.9241 ± 0.0040	0.132 ± 0.005	8.1 ± 0.2	89.7 ± 5.0	1.67	5	3b
C-14	1.4770 ± 0.0001	680.4234 ± 0.0005	0.149 ± 0.005	3.2 ± 0.3	64.6 ± 2.0	0.26	5	1
C-15	1.3735 ± 0.0001	743.8705 ± 0.0005	0.185 ± 0.004	3.0 ± 0.1	77.2 ± 0.7	0.32	3	1
C-16	6.5912 ± 0.0001	346.4303 ± 0.0005	0.227 ± 0.003	12.7 ± 0.3	89.5 ± 0.5	0.50	2	2
C-17		692.2607 ± 0.0005	0.209 ± 0.003		77.2 ± 2.0	0.07	1	2
C-18	0.9997 ± 0.0001	743.0309 ± 0.0005	0.266 ± 0.003	4.4 ± 0.5	79.3 ± 2.0	0.10	6	3b
C-19	0.8972 ± 0.0001	402.1343 ± 0.0005	0.194 ± 0.003	7.9 ± 0.5	84.2 ± 2.0	0.37	11	2
C-20	11.3840 ± 0.0002	406.1299 ± 0.0005	0.214 ± 0.002	28.3 ± 0.8	89.5 ± 0.1	0.17	2	2
C-21		406.0146 ± 0.0005	0.225 ± 0.002		97.4 ± 0.1	1.30	1	2
C-22		715.9622 ± 0.0005	0.235 ± 0.002		79.0 ± 0.1	0.19	1	2
C-23		717.1168 ± 0.0005	0.265 ± 0.002		82.3 ± 0.1	0.36	1	3b
C-24	0.5035 ± 0.0002	1045.2148 ± 0.0005	0.085 ± 0.002	9.4 ± 0.5	85.4 ± 0.1	1.26	10	3a
C-25	0.6666 ± 0.0002	1045.4059 ± 0.0005	0.175 ± 0.002	7.7 ± 0.5	83.8 ± 0.1	0.06	11	3b
C-26	1.4907 ± 0.0002	1046.0892 ± 0.0005	0.134 ± 0.002	5.7 ± 0.5	89.9 ± 0.1	0.05	4	3b
C-27		1059.2105 ± 0.0005	0.089 ± 0.002		88.4 ± 0.1	0.38	1	3a
C-28	0.4184 ± 0.0002	1061.2937 ± 0.0005	0.128 ± 0.002	6.9 ± 0.5	82.4 ± 0.1	0.06	32	3a
C-29	1.0981 ± 0.0002	1062.1106 ± 0.0005	0.073 ± 0.002	9.1 ± 0.5	87.2 ± 0.1	0.03	12	3b
C-30	1.2079 ± 0.0002	1061.2238 ± 0.0005	0.174 ± 0.002	3.9 ± 0.5	78.3 ± 0.1	0.00	13	3b
C-31	1.2992 ± 0.0002	1061.4841 ± 0.0005	0.056 ± 0.002	9.8 ± 0.5	91.3 ± 5.0	0.05	9	3a
C-32	1.4178 ± 0.0002	1061.8408 ± 0.0005	0.109 ± 0.002	9.0 ± 0.5	88.9 ± 5.0	0.17	11	3a
C-33	1.5655 ± 0.0002	1061.7487 ± 0.0005	0.070 ± 0.002	5.7 ± 0.5	81.9 ± 5.0	0.00	10	3b
C-34	1.6624 ± 0.0002	1062.4008 ± 0.0005	0.101 ± 0.002	6.3 ± 0.5	84.9 ± 5.0	0.03	8	3b
C-35	2.0925 ± 0.0002	1061.7192 ± 0.0005	0.093 ± 0.002	6.3 ± 0.5	84.2 ± 5.0	0.75	9	3a
C-36	2.1490 ± 0.0002	1062.2811 ± 0.0005	0.194 ± 0.002	2.7 ± 0.5	69.4 ± 5.0	0.00	7	3b
C-37	2.3420 ± 0.0002	1062.7525 ± 0.0005	0.163 ± 0.002	6.3 ± 0.5	82.2 ± 5.0	0.31	6	3a
C-38	2.7545 ± 0.0002	1063.2574 ± 0.0005	0.139 ± 0.002	6.3 ± 0.5	86.3 ± 5.0	0.25	6	3a
C-39	3.2365 ± 0.0002	1061.7381 ± 0.0005	0.113 ± 0.002	6.3 ± 0.5	82.3 ± 5.0	0.00	4	3b
C-40	3.2990 ± 0.0002	1062.3076 ± 0.0005	0.119 ± 0.002	3.1 ± 0.5	75.0 ± 5.0	0.06	4	3b
C-41	3.5870 ± 0.0002	1064.7338 ± 0.0005	0.202 ± 0.002	2.9 ± 0.5	72.3 ± 5.0	0.04	4	3b
C-42	5.2659 ± 0.0002	1064.6233 ± 0.0005	0.126 ± 0.002	4.2 ± 0.5	82.2 ± 5.0	0.01	2	3b
C-43	6.9791 ± 0.0002	1066.9073 ± 0.0005	0.179 ± 0.002	4.9 ± 0.5	80.5 ± 5.0	0.24	3	3b

Notes. T_C: time of transit, r_p: radius of the planet, $R_\star$: radius of the star, a: the semi-major axis, i: inclination of the orbit.
[a](1): good planet candidate, (2): stellar binaries, (3): unsettled case, (3a) suspected good candidate and (3b) suspected stellar binary candidates.

measurements, we found that the host star is a dwarf with a $T_{\rm eff}$ of 6140 ± 200 K, log g of 4.41±0.20 and [Fe/H] of 0.01±0.4. HARPS measurements conducted, under good seeing conditions, on 2013 June 24 and 25, corresponding to ASTEP phases of 0.27 and 0.68, respectively, show no significant RV variation at the 70 m s^{-1} level. This corresponds to a Saturn-type planet. However, more accurate well-sampled RV observations are needed to confirm the planetary nature of this candidate and to reach a good estimation of its mass. In addition, the stellar density ratio *versus* transit depth relation of this candidate agrees well with that for known exoplanets as described by Tingley et al. (2011).

C-3 (A-009-3827-0876, UCAC4 220-040923), which is located in the field F-01, is relatively faint (V = 16.5 mag) and has no close companion (up to V = 17 mag). The closest bright (V = 14–15 mag) stars UCAC4 220-090922 and UCAC4 220-090913 are located at more than 6 arcsec from this target. We detected 12 transit events with a depth of 1.15 per cent, a period of 1.0548 d and transit duration of 1.544 h (Fig. 17). The parent star is a dwarf ($T_{\rm eff}$ = 6680±200 K, log g = 4.00±0.1) and [Fe/H] of 0.10±0.4. No significant RV variation at the 5 km s^{-1} level was found. We need an RV point at phase 0.25 and more accurate RV observations to confirm the nature of this candidate which has a density *versus* transit depth relation close to that of known exoplanets.

C-14 (A-037-2105-3878, UCAC4 175-188215). We detected five transit events of this relatively bright star (V = 14.6 mag) located in the field F-07. The ASTEP 400 light curve shows a 2.15 per cent deep transit occurring every 1.4770 d and transit duration of 1.804 h (Fig. 17). From ANU spectroscopy, we classified this candidate as dwarf ($T_{\rm eff}$ = 5940±200 K, log g = 4.00±0.1 and [Fe/H] of −0.01±0.4). Two observations with HARPS were carried out on

Table 6. Stellar and planetary parameters of followed-up ASTEP 400 exoplanet candidates.

Cand.	M_* ($M_\odot$)	R_* ($R_\odot$)	$\log(g_*)$ (cgs)	$T_{\rm eff}$ (K)	[Fe/H]	a (au)	$r_{\rm p}$ ($R_{\rm J}$)	$T_{\rm eq}$ (K)	b
C-2	1.14 ± 0.15	1.10 ± 0.20	4.41 ± 0.20	6140 ± 200	0.01 ± 0.4	0.0370 ± 0.0015	0.75 ± 0.2	1610 ± 150	0.68 ± 0.05
C-3	1.53 ± 0.14	2.06 ± 0.09	4.00 ± 0.10	6680 ± 200	0.10 ± 0.4	0.0234 ± 0.0005	4.65 ± 0.2	3020 ± 110	1.34 ± 0.02
C-4	0.92 ± 0.11	1.84 ± 0.12	3.88 ± 0.05	5010 ± 200	−0.52 ± 0.4	0.0138 ± 0.0005	2.10 ± 0.2	2780 ± 130	1.13 ± 0.10
C-5	0.67 ± 0.09	1.60 ± 0.12	3.88 ± 0.10	4220 ± 200	−0.61 ± 0.4	0.0131 ± 0.0005	1.85 ± 0.2	2240 ± 120	1.45 ± 0.04
C-6	1.19 ± 0.13	1.24 ± 0.08	4.33 ± 0.05	6690 ± 200	−0.50 ± 0.4	0.0606 ± 0.0020	1.93 ± 0.2	1457 ± 60	0.85 ± 0.02
C-7	0.81 ± 0.10	0.93 ± 0.07	4.41 ± 0.05	5270 ± 200	−0.51 ± 0.4	0.0408 ± 0.0015	1.94 ± 0.2	1211 ± 60	0.65 ± 0.01
C-8	1.25 ± 0.13	2.17 ± 0.08	3.87 ± 0.05	6080 ± 200	−0.52 ± 0.4	0.0308 ± 0.0010	3.12 ± 0.1	2457 ± 80	0.36 ± 0.40
C-10	0.92 ± 0.10	1.50 ± 0.11	4.05 ± 0.05	5310 ± 200	−0.55 ± 0.4	0.0221 ± 0.0008	2.75 ± 0.2	2110 ± 100	1.50 ± 0.20
C-12	1.24 ± 0.20	4.93 ± 0.60	3.15 ± 0.10	4270 ± 200	−0.02 ± 0.4	0.0463 ± 0.0020	3.33 ± 0.5	2120 ± 150	1.46 ± 0.10
C-14	1.26 ± 0.15	1.85 ± 0.20	4.00 ± 0.10	5940 ± 200	−0.01 ± 0.4	0.0274 ± 0.0020	2.69 ± 0.5	2350 ± 150	1.36 ± 0.10
C-15	1.21 ± 0.15	1.83 ± 0.10	4.00 ± 0.05	6190 ± 200	−0.45 ± 0.4	0.0258 ± 0.0009	3.30 ± 0.2	2520 ± 90	0.67 ± 0.02
C-16	1.07 ± 0.12	1.19 ± 0.06	4.30 ± 0.03	6260 ± 200	−0.56 ± 0.4	0.0704 ± 0.0025	2.62 ± 0.1	1242 ± 40	0.13 ± 0.10
C-17	1.73 ± 0.20	4.00 ± 0.18	3.48 ± 0.03	6050 ± 200	−0.08 ± 0.4	0.0489 ± 0.0016	8.14 ± 0.4	2638 ± 90	0.58 ± 0.04
C-20	1.31 ± 0.15	0.83 ± 0.04	4.75 ± 0.05	6940 ± 200	−0.05 ± 0.4	0.1084 ± 0.0040	1.71 ± 0.1	921 ± 30	0.25 ± 0.03

Note. a: the semi-major axis, $r_{\rm p}$: radius of the planet, $T_{\rm eq}$: equilibrium temperature and *b*: impact parameter.

2013 June 25 and 27, which corresponds to ASTEP phases of 0.76 and 0.12, respectively. No significant RV variation at a 50 m s^{-1} level was detected. As for C-2, this corresponds to a Saturn-type planet. More accurate RV observations at different orbital phases are needed to confirm the planetary nature of this candidate and to reach a good estimation of its mass. In addition, the density *versus* transit depth relation of this target agrees very well with that of an exoplanet system. There is no bright source close to this candidate.

C-15 (A-045-2152-2821, UCAC4 185-192986). We detect five transit events of this relatively bright ($V = 13.0$ mag) candidate located in the field F-12. C-15 has a 3.29 per cent deep transit signal, a period of 1.3735 d and transit duration of 4.063 h (Fig. 17). A period of 2.7470 d is also suspected for this candidate. From ANU spectroscopic measurements, we classify this star as dwarf, with $T_{\rm eff} = 6190 \pm 200$ K and $\log g = 4.00 \pm 0.05$, and found no significant RV variation at the 2 km s^{-1} level. We classified this target as a good candidate which requires more accurate RV observations, even if its density *versus* transit depth relation does not agree well with that of an exoplanet. There is a close-by faint companion ($V = 18$ mag) 2 arcsec away.

7 SUMMARY AND CONCLUSIONS

ASTEP 400 is a 40 cm fully computer-controlled telescope providing near-continuous photometric observations in the visible during the Antarctic polar night. ASTEP 400 was designed to withstand the harsh climatic conditions at Dome C and dedicated to finding and characterizing transiting exoplanets with a photometric accuracy of a fraction of millimagnitude over a time-scale duration of a typical exoplanet transit. From its installation in 2010, to its repatriation in 2014, ASTEP 400 was improved continuously to minimize human interventions with the goal of achieving a full robotization of the instrument.

Data of the first three years of operation of the instrument were fully analysed. During this period, we observed 22 stellar fields, each field being observed continuously during ∼7 to ∼30 d, from March up to the end of September of each season, and acquired a total of 5845 h of science exposure frames. We achieved an average duty cycle of 65.14 per cent per year demonstrating that ASTEP 400 is well suited for a dedicated photometric follow-up.

We used a custom OIS data reduction pipeline and achieved a photometric precision of ∼2 and ∼20 mmag with a cadence of less than 2 min, for the brightest ($R \sim 12$ mag) and faintest ($R \sim 17$ mag) stars, respectively. We found that a large amount of correlated noise is present in our data, at all time-scales, particularly for the brightest stars. This is due to the systematic errors that affect our data.

To provide an understanding of the origin of the correlated noise, we performed a search for correlations of the rms noise with a large number of external parameters, including sky brightness due to the Sun elevation and Moon phases, FWHM PSFs, mirror defrosting temperature variations, etc. The source of the correlated noise is not obvious and does not depend on a single parameter. The influence of the sky brightness can be neglected if we start observing when the Sun is 13° below the horizon (10° for $R = 12$ mag stars) and if we excluded observations conducted 2 to 3 d before and after the full Moon. There is no evident correlation of the rms noise with tracking defects and telescope's jitter nor with hour angle, and the contribution of the blowing snow to the seeing is difficult to quantify. On the other hand, one feature is that PSF FWHMs are substantially broad. This is probably due to a combination of instrumental effects (e.g. astigmatism, thermally induced defocus, beam de-collimation turbulence on the optical path, etc.) and poor seeing on the ground, specific to the high Antarctic plateau.

We performed a BLS period search on each light curve and selected 43 planetary candidates. 20 of these candidates were observed using spectroscopic follow-up. We found four good planet candidates that will require future more accurate well-sampled RV measurements to confirm their planetary nature and to perform their complete characterization. 15 candidates were rejected as spectroscopic binaries or background EcBs. In addition, from candidates for which spectroscopic measurements have not been performed and according to their transit depth and density ratio *versus* transit depth relations, we found nine targets as good planet candidates that require future follow-up. On the other hand, we detected about 1100 new southern variable stars and more than 600 EcBs, which will be the subject of a forthcoming paper.

ASTEP 400 is the first optical telescope to have functioned nearly continuously during four year in the extreme conditions of the Antarctic plateau. Our results demonstrate the high potential of ASTEP 400, installed at Dome C in Antarctica, to obtain extremely accurate near-continuous photometric observations and monitoring several thousands of stars. In spite of these very promising results, we were not able to reach its nominal photometric precision and were not able to determine precisely the origin of the correlated

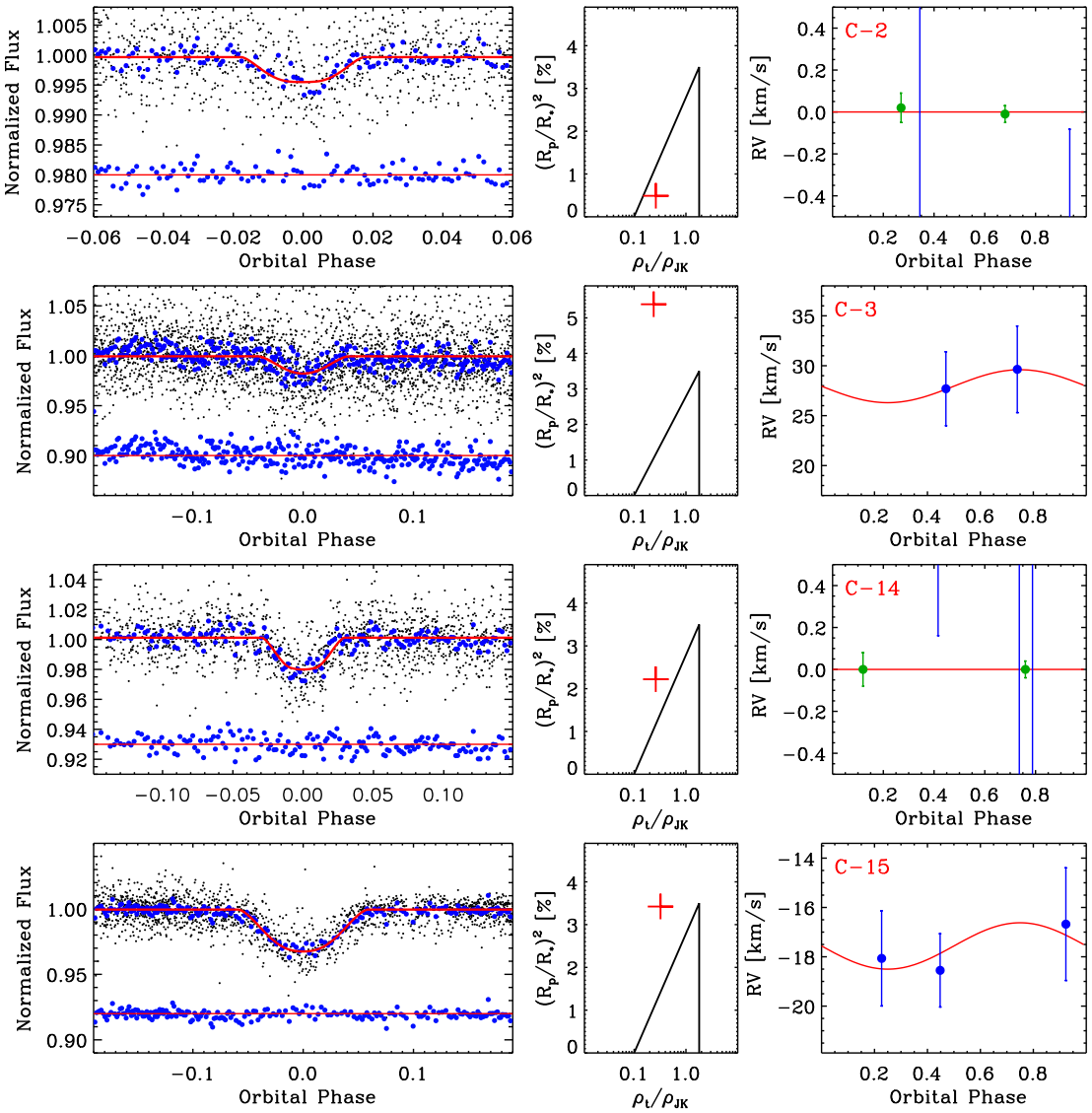

Figure 17. Normalized and phase-folded light curve, ρ_t/ρ_{JK} *versus* transit depth relation and RV measurements of the identified good planet candidates. For each light curve, the phase-folded transit is compared to the best-fitting model using transit parameters listed in Table 5 (residuals of the fit are plotted at the bottom of the figure, offset from zero). RV measurements are presented together with a rough adjustment of an orbital solution, assuming a circular orbit. For transit light curves, the grey and blue dots correspond to the original data and to the binned data at 16 exposure time units, respectively. For RV curves, blue and green (when available) dots correspond to ANU and HARPS data observations, respectively. For C-2 and C-14, the RV axes scale had been chosen to show the error bars of HARPS data and thus ANU data error bars go beyond the plot.

noise present in our data. However, we identified some ways to increase the photometric accuracy of the instrument by avoiding, or at least reducing, these instrumental and atmospheric disturbances (Guillot et al. 2015). These improvements, which should equip any future telescope operating in Antarctica, are mainly related to the ventilation of mirrors with a laminar flow and heating only their reflective parts with a temperature of 1–2°C above the ambient; a real-time adjustment of the focal position of the telescope as this position depends on the temperature; a fine alignment of the optical elements independently of the telescope position; and finally, by putting the telescope at a higher elevation and using a tip-tilt system.

However, in the present context of exoplanetary science and the arrival of space missions focused on the discovery of small planets orbiting bright nearby stars, photometric follow-up observations will be needed for validation or for joint observations at different wavelengths. In parallel, the ASTEP project has demonstrated that a robotic telescope can be operated from the Antarctic plateau with minimal interventions and provide nearly continuous observations of southern stars during the polar winter. The high data quality of ASTEP 400 light curves allowed us to detect the secondary eclipse of WASP-19b after one month of continuous observations (Abe et al. 2013). Hence, we believe that further observation campaigns from Antarctica should probably focus on the characterization of known transiting exoplanets rather than on discovery surveys.

ACKNOWLEDGEMENTS

The ASTEP project has been funded by the French *Agence Nationale de la Recherche* (ANR), *Institut des Sciences de l'Univers* (INSU), *Programme National de Planétologie* (PNP), *Institut Paul-Émile Victor* (IPEV), and the *Plan Pluri-Formation* OPERA

between *Observatoire de la Côte d'Azur* and *Université de Nice Sophia Antipolis* (UNS). The field activities at Dome C benefited from the support of the French and Italian polar agencies IPEV and PNRA in the framework of the Concordia station programme. We would like to thank F. Valbousquet from our industrial partner *Optique et Vision* for his invaluable support in the development of the instrument. AA, DM and EA would like to thank the winter-over DC6 and DC7 Concordia crews, particularly A. Le Forestier, I. Bourgeois, D. Colin, A. Galeandro, V. Koutcheroff, P. Robert and E. MacDonald for their continuous and timely support during the winter-over. IG is funded by INSU/CNRS. We wish to thank the anonymous referee for insightful comments that significantly improved the clarity of the paper.

REFERENCES

Abe L. et al., 2013, A&A, 553, A49
Alard C., Lupton R. H., 1998, ApJ, 503, 325
Andersen M. I., Freyhammer L., Storm J., 1995, in Benvenuti P., ed., ESO Conf. Workshop Proc., Vol. 53, Calibrating and Understanding HST and ESO Instruments. European Southern Observatory, Garching, p. 87
Aristidi E., Agabi A., Vernin J., Azouit M., Martin F., Ziad A., Fossat E., 2003, A&A, 406, L19
Aristidi E. et al., 2005, A&A, 430, 739
Aristidi E. et al., 2009, A&A, 499, 955
Ashley M. C. B., Burton M. G., Lawrence J. S., Storey J. W. V., 2004, Astron. Nachr., 325, 619
Ashley M. C. B., Burton M. G., Calisse P. G., Phillips A., Storey J. W. V., 2005, Highlights Astron., 13, 932
Bachelet E. et al., 2012, ApJ, 754, 73
Baranne A. et al., 1996, A&AS, 119, 373
Bayliss D. et al., 2013, AJ, 146, 113
Bonner C. S. et al., 2010, PASP, 122, 1122
Chapellier E. et al., 2016, preprint (arXiv:e-prints)
Collier Cameron A. et al., 2007, MNRAS, 380, 1230
Crouzet N., Guillot T., Fressin F., Blazit A., A STEP Team, 2007, Astron. Nachr., 328, 805
Crouzet N. et al., 2010, A&A, 511, A36
Crouzet N. et al., 2013, in Burton M. G., Cui X., Tothill N. F. H., eds, Proc. IAU Symp. 288, Astrophysics from Antarctica. Cambridge Univ. Press, Cambridge, p. 226
Daban J.-B. et al., 2010, Proc. SPIE, 7733, 77334T
Dempsey J. T., Storey J. W. V., Phillips A., 2005, PASA, 22, 91
Dopita M., Hart J., McGregor P., Oates P., Bloxham G., Jones D., 2007, Ap&SS, 310, 255
Dopita M. et al., 2010, Ap&SS, 327, 245
Eastman J., Gaudi B. S., Agol E., 2013, PASP, 125, 83
Fossat E., Aristidi E., Agabi A., Bondoux E., Challita Z., Jeanneaux F., Mékarnia D., 2010, A&A, 517, A69
Fressin F., Guillot T., Morello V., Pont F., 2007, A&A, 475, 729
Frezzotti M. et al., 2005, J. Glaciol., 51, 113
Fruth T. et al., 2014, PASP, 126, 227
Gazak J. Z., Johnson J. A., Tonry J., Dragomir D., Eastman J., Mann A. W., Agol E., 2012, Adv. Astron., 2012, 697967
Giordano C., Vernin J., Chadid M., Aristidi E., Agabi A., Trinquet H., 2012, PASP, 124, 494
Guillot T. et al., 2015, Astron. Nachr., 336, 638
Kenyon S. L., Storey J. W. V., 2006, PASP, 118, 489
Kenyon S. L., Lawrence J. S., Ashley M. C. B., Storey J. W. V., Tokovinin A., Fossat E., 2006, PASP, 118, 924
Kovács G., Zucker S., Mazeh T., 2002, A&A, 391, 369
Kovács G., Bakos G., Noyes R. W., 2005, MNRAS, 356, 557
Lang D., Hogg D. W., Mierle K., Blanton M., Roweis S., 2010, AJ, 139, 1782
Lawrence J. S., Ashley M. C. B., Tokovinin A., Travouillon T., 2004, Nature, 431, 278
Mandel K., Agol E., 2002, ApJ, 580, L171
Mazeh T. et al., 2009, A&A, 506, 431
Miller J. P., Pennypacker C. R., White G. L., 2008, PASP, 120, 449
Montalto M. et al., 2007, A&A, 470, 1137
Moore A. et al., 2008, Proc. SPIE, 7012, 701226
Mosser B., Aristidi E., 2007, PASP, 119, 127
Munari U., Sordo R., Castelli F., Zwitter T., 2005, A&A, 442, 1127
Pepe F. et al., 2002, The Messenger, 110, 9
Petenko I. et al., 2014, A&A, 568, A44
Pont F., Zucker S., Queloz D., 2006, MNRAS, 373, 231
Rauer H., Fruth T., Erikson A., 2008, PASP, 120, 852
Robin A. C., Reylé C., Derrière S., Picaud S., 2003, A&A, 409, 523
Rupprecht G. et al., 2004, in Moorwood A. F. M., Iye M., eds, Proc. SPIE Conf. Ser. Vol. 5492, Ground-based Instrumentation for Astronomy. SPIE, Bellingham, p. 148
Santerne A. et al., 2015, MNRAS, 451, 2337
Schlegel D. J., Finkbeiner D. P., Davis M., 1998, ApJ, 500, 525
Smith A. M. S. et al., 2012, A&A, 545, A93
Strassmeier K. G. et al., 2008, A&A, 490, 287
Tamuz O., Mazeh T., Zucker S., 2005, MNRAS, 356, 1466
Tingley B., Bonomo A. S., Deeg H. J., 2011, ApJ, 726, 112
Trinquet H., Agabi A., Vernin J., Azouit M., Aristidi E., Fossat E., 2008, PASP, 120, 203
Wang L. et al., 2011, AJ, 142, 155

This paper has been typeset from a TEX/LATEX file prepared by the author.